Complex aneuploidy triggers autophagy and p53-mediated apoptosis and impairs the second lineage segregation in human preimplantation embryos

Marius Regin[1], Yingnan Lei[1], Edouard Couvreu De Deckersberg[1], Yves Guns[2], Pieter Verdyck[3], Greta Verheyen[2], Hilde Van de Velde[2,4], Karen Sermon[1,#], Claudia Spits[1,#,*]

[1]Research Group Reproduction and Genetics, Faculty of Medicine and Pharmacy, Vrije Universiteit Brussel, Laarbeeklaan 103, 1090 Jette, Brussels, Belgium

[2]Brussels IVF, Universitair Ziekenhuis Brussel, Laarbeeklaan 101, 1090 Jette, Brussels, Belgium

[3]Vrije Universiteit Brussel (VUB), Universitair Ziekenhuis Brussel (UZ Brussel), Clinical Sciences, Research Group Reproduction and Genetics, Centre for Medical Genetics, Brussels, Belgium

[4]Research Group Reproduction and Immunology, Faculty of Medicine and Pharmacy, Vrije Universiteit Brussels, Laarbeeklaan 103, 1090 Jette, Brussels, Belgium

[#]These authors contributed equally to this work.

*Corresponding author: Claudia.Spits@vub.be

ABSTRACT

Aneuploidy is present in about 80% of human preimplantation embryos and is thought to largely explain our relatively low fertility. However, the percentage of aneuploid cells decreases progressively during the early cleavages and chromosomally mosaic human embryos have been shown to result in healthy new-borns with normal karyotypes. These observations imply a selective loss of aneuploid cells, but the underlying mechanisms are not yet fully understood in human embryos. From studies in mouse embryos and human 2D gastruloids we know that aneuploid cells are eliminated from the epiblast by apoptosis and rather tolerated in the trophectoderm and that aneuploid cells show proteotoxic stress, autophagy and p53 activation. Here, we show that, complex aneuploid human blastocysts present proteotoxic stress, autophagy, deregulated p53 signalling and apoptosis in the trophectoderm and show impaired development of the epiblast and the primitive endoderm. Our findings explain why fully aneuploid embryos fail to further develop and shed light on the mechanisms by which aneuploid cells are removed from mosaic human embryos.

Introduction

Aneuploidy is common in human preimplantation embryos from both natural (Munné *et al.*, 2020a) and medically assisted reproduction cycles (Voullaire *et al.*, 2000; Wells and Delhanty, 2000; Vanneste *et al.*, 2009; Johnson *et al.*, 2010; Chavez *et al.*, 2012; Mertzanidou *et al.*, 2013b, 2013a; Chow *et al.*, 2014; Fragouli *et al.*, 2019; Popovic *et al.*, 2020; Starostik *et al.*, 2020; Capalbo *et al.*, 2021; Yang *et al.*, 2021). Depending on the study, up to 80% of human cleavage stage embryos are found to be aneuploid, of which 70% show chromosomal mosaicism, i.e. the presence of at least two cell lineages with different genomic content (Regin *et al.*, 2022). The reasons behind this high rate of chromosomal abnormalities of mitotic origin is still largely unknown (McCoy, 2017) but could be a combination of a weak spindle assembly checkpoint (SAC) that is uncoupled of apoptosis until the blastocyst stage (Jacobs *et al.*, 2017; Vázquez-Diez *et al.*, 2019), in combination with an abundancy of transcripts of anti-apoptotic genes in cleavage-stage embryos (Yan *et al.*, 2013). After embryonic genome activation, the rapidly increasing expression of pro-apoptotic genes along with the full functionality of the SAC establishes the control of mitotic errors.

It is by now well established that chromosomally mosaic embryos can result in healthy new-borns with normal karyotypes, implying a progressive and selective loss of aneuploid cells during development (Greco *et al.*, 2015; Fragouli *et al.*, 2017, 2019; Munné *et al.*, 2017, 2020b; Capalbo *et al.*, 2021; Viotti *et al.*, 2021; Yang *et al.*, 2021). In the preimplantation embryo, several studies have shown that the proportion of aneuploid cells within the embryo decreases three days post fertilization (3dpf) (van Echten-Arends *et al.*, 2011; Fragouli *et al.*, 2019; Yang *et al.*, 2021) with no apparent preferential allocation of aneuploid cells during the first lineage segregation

event to either trophectoderm (TE) or inner cell mass (ICM) (Capalbo *et al.*, 2013; Popovic *et al.*, 2018; Starostik *et al.*, 2020; Ren *et al.*, 2022). However, aneuploid cells can be excluded as cell debris (Orvieto *et al.*, 2020) or allocated to the blastocoel cavity and to peripheral cells that do not participate in the formation of the embryo (Griffin *et al.*, 2022). In some studies, (Starostik *et al.*, 2020; Griffin *et al.*, 2022) the TE contained a slightly higher number of aneuploid cells than the ICM, without reaching statistical significance. In their landmark paper, (Bolton *et al.*, 2016) found a quite similar but statistically significant 6% TE enrichment in mouse embryos treated with the SAC inhibitor reversine to induce mosaic aneuploidy. This small enrichment fell in the same confidence interval as the Starostik study, therefore TE enrichment cannot be ruled out in the human embryo. After implantation, aneuploid cells become progressively more frequent in the trophoblast lineage which is derived from TE cells as compared to the epiblast (EPI) and primitive endoderm (PrE) lineages which are derived from the ICM cells during the second lineage segregation (Starostik *et al.*, 2020). This suggests that the trophoblast cells are more tolerant to aneuploidy, in line with the rate of 1-2% of confined placental mosaicism observed in ongoing pregnancies in the general population (Kalousek and Vekemans, 1996) and with the presence of aneuploid cells in the placental lineages only (Zamani Esteki et al., 2019). This is further supported by a recent study showing that genetic mosaicism is a normal feature of the placenta and is due to genetic bottlenecks that occur early in development (Coorens *et al.*, 2021). Taken together, strong evidence supports the selective elimination of aneuploid cells from the embryonic lineage in the pre- and post-implantation development, while the placenta appears to be more tolerant to genetic imbalances.

From a mechanistic point of view, this selective clearance is thought to be mediated by two intracellular stress responses that have been particularly well studied in cancer aneuploidy and in yeast models (reviewed in Santaguida and Amon, 2015; Zhu et al., 2018). First, aneuploidy results in gene-dosage defects, leading to an unbalanced protein pool and proteotoxic stress (Oromendia *et al.*, 2012; Ohashi *et al.*, 2015). If this remains unresolved by activation of autophagy, CASP8/LC3B/p62 will interact to activate the apoptosis cascade (Pan *et al.*, 2011; Stingele *et al.*, 2012; Dürrbaum *et al.*, 2014). Second, aneuploidy results in replication stress that can lead to DNA-damage, resulting in *p53* activation and ultimately to apoptosis (Zhu *et al.*, 2018; Regin *et al.*, 2022). Bolton *et al*. (Bolton *et al.*, 2016) showed that aneuploid cells are selectively cleared from chimeric mouse embryos generated from control blastomeres mixed with aneuploid blastomeres obtained using a treatment with the SAC inhibitor reversine. Later work by the same group showed that apoptosis of these aneuploid cells requires autophagy and *p53* activation and that euploid cells in the mouse embryo compensate this cell loss by increased proliferation (Singla *et al.*, 2020). The authors proposed that the proteotoxic stress in these aneuploid chimeric mouse embryos activated the p53 pathway, which in turn activated autophagy and apoptosis. In a recent study using human 2D gastruloids with reversine-induced aneuploidy, apoptosis was only induced in differentiating but not in pluripotent cells, although aneuploidy induced an increase in total nuclear p53 proteins (Yang *et al.*, 2021). The apoptotic response to aneuploidy also seems to be lineage-specific. In the mouse, aneuploid cells in the ICM are eliminated by apoptosis while they are rather tolerated in the TE (Bolton *et al.*, 2016). Furthermore, in a follow-up study, (Singla *et al.*, 2020) demonstrated that during the peri-implantation period, aneuploid cells were eliminated from the EPI and the PrE in similar rates, and that the EPI-specific elimination of aneuploid cells by apoptosis is coupled to increased

proliferation rates of euploid cells. Similarly, in human gastruloids, aneuploid cells are eliminated by apoptosis from the embryonic germ layers but are tolerated in the TE-like cells (Yang *et al.*, 2021).

The type of aneuploidy and the percentage of aneuploid cells within a euploid/aneuploid mosaic embryo determine its developmental capacity. The viability of mouse embryos inversely correlates to the proportion of aneuploid cells, with 50% of euploid cells being sufficient to sustain normal development (Bolton *et al.*, 2016). This same threshold appears to apply to human embryos, where embryos with less than 50% of aneuploid cells have higher developmental potential than those containing more than 50%, albeit both performing worse than fully euploid embryos (Viotti et al., 2021, Capalbo et al., 2021). Conversely, whole chromosome gains and losses that are present in every cell of the human embryo are usually linked to lethality with the notable exception of trisomies 13 (Patau syndrome), 18 (Edwards syndrome) and 21 (Down syndrome), and sex chromosome abnormalities. Shahbazi et al. recently described the consequences of carrying specific meiotic aneuploidies on human embryo development using an *in vitro* implantation model (Shahbazi *et al.*, 2020). They showed that human embryos with trisomy 15, 16 and 21 and monosomy 21 readily all reached the blastocyst stage, and that monosomy 21 embryos arrested after implantation while trisomy 15 and 21 embryos developed further. Interestingly, trisomy 16 embryos showed a hypoproliferative trophoblast due to excessive *CDH1* expression, a gene located on chromosome 16.

In this study, we investigated the cellular consequences of aneuploidy during human preimplantation development, with a focus on stress response and lineage segregation events. We studied embryos with complex meiotic aneuploidy rather than mosaic embryos to ascertain that our observations were significant.

Methods

Ethical approval. All experiments have been approved by the local Commission of Medical Ethics of the UZ Brussel (B.U.N. 143201628722) and the Federal Committee for Medical and Scientific Research on Human Embryos *in vitro* (AdV069 and AdV091). Patients from Brussels IVF (UZ Brussel) donated their embryos for research after written informed consent.

Culture of human pre-implantation embryos. We warmed vitrified human blastocysts (5-6dpf) after PGT or at 3dpf using the Vitrification Thaw Kit (Vit Kit-Thaw; Irvine Scientific, USA) following manufacturer's instructions. Embryos were graded before vitrification according to Gardner and Schoolcraft criteria (Gardner and Schoolcraft, 1999). Post PGT-embryos were left to recover for 2h in 25 µL droplets of Origio Sequential Blast™ medium (Origio) at 37°C with 5% O_2, 6% CO_2 and 89% N_2, after which they underwent a second TE biopsy (Fig. 1a). For the reversine experiment, we cultured the 3dpf embryos for 24h in the same medium supplemented with 0.5 µM reversine (Stem Cell Technologies) and after wash-out we let them develop until 5dpf and subsequently took a biopsy (Fig. 1b). The PGT embryos used for the second experiment series (Fig. 4a) were cultured for 16h after warming to allow them to progress to the second lineage. Prior to fixation we live-stained all the embryos with either Caspase-3/7 or Caspase-8 (Supplementary Table 30) for 30 min and subsequently removed the zona pellucida using Acidic Tyrode's Solution (Sigma-Aldrich) for 30 sec – 2 min and subsequently washed in PBS/2%BSA.

Biopsy procedure. The zona pellucida was opened (15-25µm) on 4dpf using a Saturn Laser (Cooper Surgical). For PGT cycles**,** expanded good quality embryos

were biopsied on 5dpf; early blastocysts were evaluated again for expansion on 6dpf. Briefly, embryos were transferred to HEPES buffered medium and biopsied on a Nikon inversed microscope equipped with a Saturn Laser. The herniated TE cells were then aspirated and cut using manual laser shoots. In case of sticking cells this was supported by mechanical cutting. After successful tubing, the blastocysts were vitrified using CBS-VIT High-Security straws (CryoBioSystem, L'Aigle, France) with dimethylsulphoxide-ethylene glycol-sucrose as the cryoprotectants (Irvine Scientific Freeze Kit, Newtownmountkennedy, County Wicklow, Ireland) (Van Landuyt *et al.*, 2011). The TE biopsy for RNA-sequencing (Fig. 1a,b) was performed with the same procedure, cells were biopsied form the same opening in the zona pellucida.

PGT. During PGT we analyzed a TE sample with multiple cells for each embryo. Next Generation Sequencing: The chromosomal analysis was performed by WGA (Sureplex, Illumina) followed by library preparation (KAPA HyperPlus, Roche), sequencing on a NovaSeq (Illumina) and an *in-house* developed interpretation pipeline. The analysis has an effective resolution of 5 Mb.

SNP-array: We relied on whole genome amplification (MDA, Repli-G) followed by genome wide SNP array using Karyomapping (Vitrolife) with Bluefuse software (Vitrolife). In addition, SNP array data were analyzed with an *in-house* developed interpretation pipeline for aneuploidy detection.

RNA-sequencing. Multiple (5-10) TE cells were used as input to generate full length cDNA with the SMART-Seq™ v4 Ultra™ Low Input RNA Kit (Clontech Laboratories, Inc.) according to the manufacturer's instructions. The quality of cDNA was checked using the AATI Fragment Analyzer (Advances Analytical). Library preparation was performed using the KAPA HyperPlus Library Preparation Kit (KAPA Biosystems)

according to the manufacturer's instructions. During cDNA synthesis and library preparation we used 17 and 11 PCR cycles, respectively. Sequencing was performed on a NovaSeq 6000 (Illumina) with 25 million reads per sample.

Bioinformatics analysis. Reads were trimmed using cutadapt version 1.11 to remove the "QuantSEQ FWD" adaptor sequence. We checked the quality of the reads using the FastQC algorithm (Love *et al.*, 2014). Count tables were generated using STAR (Dobin *et al.*, 2013) (version 2.5.3) through mapping against the Genome Reference Consortium Human Build 38 patch release 10 (GRCh38.p10) combined with a general transfer format (GTF) file, both downloaded from the Ensembl database. The RNA-sequencing by Expectation Maximization (RSEM) (Li and Dewey, 2011) software (version 1.3.0) was used to produce the count tables.

Differential gene expression analysis was performed using R-studio (Version 1.1.456) with the edgeR (Robinson *et al.*, 2009) and limma (Ritchie *et al.*, 2015) packages. We included genes with a count per million greater than 1 in at least two samples. The trimmed mean of M values (Robinson and Oshlack, 2010) algorithm was used for normalization. The normalized counts were then transformed in a $\log_2$ fold-change ($\log_2$FC) table with their associated statistics. In each comparison, genes with a $|\log_2 FC| > 1$ and an p-value < 0.05 were considered as significantly differentially expressed.

Gene set enrichment analysis (GSEA) was performed using the 'investigate gene sets' function on the website of the Molecular Signature Database (http://www.gsea-msigdb.org/gsea/msigdb/annotate.jsp). We used all differentially expressed genes (Supplementary Tables 2, 3) as input and investigated Hallmark, C2 and C5 gene sets with FDR-q values < 0.05. For the analysis of gene dosage effects, we could

only use the TOP500 differentially expressed genes by p-value since the Molecular Signature Database changed the cut-off during the period of our data analysis (raw data, Supplementary Tables 26, 27). In the figures 1f and g we used a supervised approach and sorted the significantly deregulated gene sets by the total amount of genes in overlap. Figure 2f was also supervised but the gene sets were sorted by FDR-q value.

Ingenuity Pathway analysis (IPA, Qiagen Inc.) was used to investigate activated, deregulated and inhibited upstream regulators and canonical pathways. As for the GSEA we used all differentially expressed genes of our two test sets with their respective $\log_2$FC and p-value. For the upstream regulators IPA computes z-scores with associated p-values that are considered significant when $p < 0.05$. If significant, a z-score > 2 means activated, a z-score < 2 means inhibited and in between means deregulated. For the canonical pathways IPA computes z-scores with associated p-values that are considered significant when $p < 0.05$. If significant, we considered a z-score > 1.5 as activated, a z-score < 1.5 as inhibited and in between as deregulated. We generated all figures in a supervised approach.

Transcription factor analysis of all differentially expressed genes was performed using Enrichr (https://maayanlab.cloud/Enrichr/). We selected the outputs from ChEA 2016 and ENCODE ChEA consensus and considered those transcription factors as significant with a p-value < 0.05.

The copy number variation (CNV) analysis was inferred from our RNA-sequencing data set using *inferCNV* R package (version 1.7.1) (Inferring copy number alterations from tumor single cell RNA-Seq data (https://github.com/broadinstitute/inferCNV/wiki"). Our count table was used as input

and compared to the reference set which in our case was the expression data of the euploid embryos. The analysis followed the standard workflow in inferCNV with the following parameters: “denoise” mode, value of 1 was used for the “cutoff”, prediction of CNV states using default Hidden Markov Models (HMM) method, “cluster_by_groups” was set to TRUE, and other values were set by default.

All figures were generated using R-studio (Version 1.1.456).

Gene dosage analysis. We calculated the total number of loci with imbalanced gene expression based on the genetic abnormalities identified during the PGT. For this, we used the number of coding loci per chromosomal region as listed in the ENSMBL database (ensemble.org) and included both gains and losses, either mosaic or homogeneously present, and both full chromosomal aneuploidy as well as segmental abnormalities. The embryos were ranked based on the total number of imbalanced loci and separated into a low- and a high-imbalanced gene dosage group. The low-dosage group contained the embryos with the lowest 50th percentile in number of unbalanced loci, the high-dosage group the embryos with 50th percentile or higher (Supplementary Table 25, 29).

Immunocytochemistry. Embryos were fixed using 4% paraformaldehyde (Sigma-Aldrich) for 10 min, washed three times in PBS/2%BSA for 5 min and then permeabilized using 0.1% Triton X-100 (Sigma-Aldrich) for 20 min followed by another washing cycle. We used 10% FBS supplemented with 2% BSA for 1h to block non-specific protein binding. The embryos were then incubated overnight with primary antibodies (Supplementary Table 30) diluted in blocking buffer at 4°C. The next day, they underwent another washing cycle using PBS/2%BSA and were then incubated with secondary antibodies (1:200, Supplementary Table 26) for 1h at room

temperature. After washing, nuclei were stained using Hoechst 33342 (5µg/mL, Life Technologies) diluted in PBS/2%BSA for 15 min. For imaging we mounted the embryos on poly-L-lysine coated glass slides (Sigma-Aldrich) in 3µL of PBS. To avoid flattening of the embryos we used Secure-Seal™ Spacers (9mm diameter, 0.12mm deep, Thermofisher) before putting the coverslips in place. For the experiments that required re-staining (Fig. 4a) we imaged the embryos in 3µL PBS/2%BSA in 18 well µ-Slides (Ibidi) and subsequently recuperated them. After recuperation we photobleached the embryos stained for CASP3/7 by using maximum laser power of the 488 nm channel and maximum size of the pinhole for 10 min. The embryos were then re-stained using rat-anti-GATA4 primary antibody and the matching Alexa Fluor 488 secondary antibody (Supplementary Table 30) (to replace the CASP3/7 staining).

Imaging and image analysis. Confocal imaging was performed using the LSM800 (Zeiss). Z-stacks were taken with a LD C-Apochromat 40x/1.1 NA water immersion objective in optical sections of 1µm. Nuclei were counted using Arivis Vision 4D (3.4.0). All other measurements were performed using the Zen 2 (blue edition) software based on the optical sections and/or orthogonal projections.

Statistics. The type of statistical test and p-values are mentioned in the figure legends. For experiments that contained groups with small sample sizes we used non-parametric tests (Mann-Whitney or Kruskal-Wallis test). Fisher-exact test was used to determine the dependency of the ploidy status on the presence or absence of primitive endoderm. Otherwise we used Student's t-test with Welch's correction when we assumed normal distribution and unequal standard deviations. We used GraphPad Prism 9.0.0 or R-studio for statistical testing. The trend analysis regarding gene dosage effects was performed with SPSS using the Jonkheere-Terpstra test.

284

Results

Human embryos with meiotic complex aneuploidy show transcriptional signatures of a deregulated p53 pathway and apoptosis

We first tested the hypothesis that chromosomally unbalanced cells are cleared during human preimplantation development by apoptosis, mediated by both sustained p62-LC3B accumulation as a marker for autophagy and DNA-damage-mediated p53 activation. Fifty cryopreserved human blastocysts (5 or 6dpf) that had been previously diagnosed by Preimplantation Genetic Testing (PGT) as either euploid (n=28) or containing non-mosaic complex aneuploidy of at least two whole chromosomes and assumed of meiotic origin (except for one)(n=22, further referred to as aneuploid, Fig. 1a, Supplementary Table 1) underwent a second TE biopsy to collect cells for RNA sequencing. Eleven warmed human cleavage stage embryos that were treated with 0.5 µM reversine from 3dpf to 4dpf and further developed to the blastocyst stage (referred to as reversine-treated embryos, Fig. 1b) were also biopsied (on 5dpf or 6dpf) to serve as a comparison with the results obtained in the mouse. The concentration of 0.5 µM reversine was chosen based on previous experiments in mouse embryos (Bolton *et al.*, 2016; Singla *et al.*, 2020). Of these, 14 euploid, 20 aneuploid and 11 reversine-treated embryos (total=45) yielded good quality RNA-sequencing results.

Unsupervised hierarchical clustering and principal component analysis using all expressed genes revealed no clustering of the euploid, aneuploid or reversine-treated embryos in distinct groups (Fig. 1c, Supplementary Fig. 1a). We used InferCNV (https://github.com/broadinstitute/inferCNV/wiki") to bioinformatically infer unbalanced chromosomal copy numbers from gene expression data, based on

higher or lower expression of genes located on chromosomes with gains or losses respectively (Fig. 1d, Supplementary Fig. 1b, Supplementary Table 1). We compared the outcomes to the results obtained during PGT and found a match for 45/48 of the full chromosome aneuploidies, while euploidy was correctly predicted in all cases (Supplementary Fig. 1b). These results show that aneuploidy in human blastocysts results in significant abnormal gene dosage effects. The exact karyotypes of the reversine-treated embryos could not be determined since reversine induces different aneuploidies in each cell, leading to mosaic TE biopsies. However, InferCNV allowed us to determine a trisomy 12 meiotic chromosomal abnormality in one reversine-treated embryo (Supplementary Figure 1c), confirming that the reversine treatment causes random aneuploidy while naturally occurring meiotic aneuploidies are readily determined.

Despite the abnormal gene dosage, and in line with the lack of clear clustering in the PCA, the differential gene expression analysis yielded very few genes with a false discovery rate (FDR-q-value) under 0.05. These findings are similar to those of other studies on the transcriptome of aneuploid human embryos (Groff *et al.*, 2019; Maxwell *et al.*, 2022). Therefore, we used the differential gene expression with a cutoff value of $|\log_2 \text{ fold change}|>1$ and $-\log_{10}(\text{p-value})<0.05$, and primarily focused on pathway analysis. We found 547 upregulated and 463 downregulated genes in aneuploid versus euploid embryos (Fig. 1e, Supplementary Table 2). Amongst the top upregulated genes was Growth Differentiation Factor 15 (*GDF15*), a gene that has been found to be upregulated in human aneuploid cells (Dürrbaum *et al.*, 2014) including aneuploid human embryos (Starostik *et al.*, 2020). When comparing reversine-treated versus euploid embryos we observed 539 upregulated and 355 downregulated genes (Fig. 1f, Supplementary Table 3). While only 9.6% of the

differentially expressed genes are in common between the aneuploid and reversine-treated embryos (Fig. 1g, h, Supplementary Table 4), pathway analysis revealed several commonly deregulated pathways. We identified deregulation of the p53 pathway and apoptosis (FDR q-value < 0.05, Fig. 1i, Supplementary Tables 5, 6) and deregulation of cell population proliferation, apoptotic process, regulation of cell death, and cell cycle (Fig. 1j, Supplementary Tables 7, 8). The prediction of p53 activation is also supported by differential expression of several p53 target genes (Jaiswal *et al.*, 2021), such as *MDM2* and *PPM1D* (feedback); *CDKN1A, BTG2, GADD45A* (cell-cycle arrest); *TNFRSF10B* (apoptosis), *DDB2* and *RRM2B* (DNA-repair); *FDXR* (metabolism) and *SESN1* (translation control) (Supplementary Table 2). Other pathways of interest related to DNA damage and p53, such as cellular response to DNA damage stimulus and DNA damage response signal transduction by p53 class mediator were specific to the aneuploid group. Cellular senescence signatures in the aneuploid embryos and selective autophagy in the reversine-treated group were also deregulated (Supplementary Tables 9, 10). Ingenuity pathway analysis (IPA) showed that upstream regulators *CDK19* and *AURK* (cell cycle) and *GAS2L3* and *ANLN* (cell growth) were inhibited in the aneuploid group (Fig. 1k, Supplementary Table 11). In line with the GSEA analysis, *p53* was the most activated upstream regulator. Reversine-treated embryos activated *ATM* which is a well-known sensor of DNA-damage that mediates target genes such as *p53* (Banin *et al.*, 1998) (Fig. 1l, Supplementary Table 12). Canonical pathway analysis by IPA confirmed that p53 signalling, autophagy, cell-cycle pathways and senescence are deregulated in aneuploid embryos (Fig. 1m, Supplementary Table 13). The TE of reversine-treated embryos showed activated senescence, similar to the mouse reversine-treated embryos (Bolton *et al.*, 2016) (Fig. 1n, Supplementary Table 14).

Transcription factor analysis identified significant *p53* expression in both aneuploid and reversine-treated groups (Supplementary Tables 15, 16).

We next compared our set of differentially expressed genes to those identified by other studies investigating the gene expression of euploid and aneuploid embryos, namely: mosaic monosomies 4, 7, 10, 15, 19 and mosaic trisomies 15 and 19 (Maxwell *et al.*, 2022), trisomy 16 and monosomy 16 (Fuchs Weizman *et al.*, 2019), monosomy 21 (Sanchez-Ribas *et al.*, 2019) and embryos that contained various types of chromosomal abnormalities (Vera-Rodriguez *et al.*, 2015; Licciardi *et al.*, 2018; Starostik *et al.*, 2020) (detailed overview in Supplementary Table 17). Overall, we found modest overlaps (Supplementary Figure 1d,e, Supplementary Tables 18-20). Most commonalities were with the data of Starostik et al, where we found an overlap in 87 genes (2.3%) (Starostik *et al.*, 2020). These included target genes of the p53 pathway such as *MDM2* and *CDKN1A* (Supplementary Fig. 1d, Supplementary Table 20). Interestingly, GSEA of these 87 genes identified an enrichment of intrinsic apoptotic signalling pathway by p53 class mediator and the apoptotic signalling pathway, in line with the findings of our dataset (Supplementary Table 19).

High gene-dosage imbalances result in stronger cellular stress signatures in human embryos

To test if there was a relationship between the level of stress signatures and the size of chromosomal imbalances in embryos as previously described in cancer (Dürrbaum and Storchová, 2016), we separated the aneuploid group into a low- and a high-imbalanced gene dosage group, based on the total number of coding loci that were affected by the chromosomal abnormalities. The low-dosage group contained the

embryos under the 50th percentile when ranking the embryos from the lowest to the highest number of unbalanced loci, the high-dosage group the embryos with 50th percentile or higher (Supplementary Table 21). Hierarchical clustering using the top 500 deregulated genes showed that all high-dosage embryos clustered together and separated from the euploid embryos, while the low-dosage embryos clustered with either group (Fig. 2a). Differential gene expression with $|\log_2$ fold change$|>1$ and $-\log_{10}$(p-value)<0.05 resulted in 404 upregulated and 340 downregulated genes in low-dosage versus euploid embryos and in 716 upregulated and 627 downregulated genes in high-dosage versus euploid embryos with an overlap of 104 (10%) between both aneuploid groups (Fig. 2b-e, Supplementary Tables 22,23). We identified deregulation of TNFA signalling via NFkB, p53 pathway and apoptosis for both groups (FDR q-value < 0.05, Fig. 2f, Supplementary Tables 24,25). High-dosage embryos additionally showed an unfolded protein response, suggesting that this signature may only be present in the embryos with more and/or larger abnormal chromosomes. In the high-dosage group more of the genes of the p53 and apoptosis pathways were deregulated, and with higher significance (Fig. 2g,h, Supplementary Tables 26,27). The gene expression levels in the p53 and apoptosis pathways show a stepwise distribution between the gene dosage groups (Fig. 2i).

Aneuploidy triggers proteotoxic stress, autophagy and apoptosis in human embryos

To further investigate the cellular stress responses identified by the transcriptomic analysis, we immunostained the same embryos that underwent TE biopsy for transcriptome analysis. Thirty-seven (18 euploid, 19 aneuploid) of the 50 PGT embryos and 8 of the 11 reversine-treated embryos were successfully stained for markers of apoptosis, proteotoxic stress and autophagy (Fig. 3a,b). Aneuploid

embryos showed increased intensity levels of active CASP3/7 (13 euploid and 8 aneuploid embryos stained) and CASP8 (6 euploid, 9 aneuploid and 8 reversine-treated embryos stained) (Fig. 3c-f). Both aneuploid and reversine-treated embryos had lower cell numbers than euploid embryos (Fig. 3g). We investigated whether proteotoxic stress and autophagy (Oromendia *et al.*, 2012; Stingele *et al.*, 2012; Dürrbaum *et al.*, 2014; Ohashi *et al.*, 2015; Singla *et al.*, 2020) were also present in aneuploid human embryos. The number of puncta per cell of autophagy markers LC3B (19 euploid, 22 aneuploid and 8 reversine-treated embryos stained) and p62 (6 euploid and 9 aneuploid embryos stained) and the intensity levels of proteotoxic stress marker HSP70 (13 euploid, 8 aneuploid and 8 reversine-treated embryos stained) were significantly increased in both aneuploid and reversine-treated embryos (Fig. 3h-k). The gene expression profiles suggest that the accumulation of autophagic proteins in aneuploid embryos is caused by increased autophagic flux due to differential expression of the *p53* target gene DNA Damage Regulated Autophagy Modulator-1 (*DRAM1*), rather than by inhibition of autophagy (Supplementary Table 2). DRAM1 is located in the lysosomal membrane and it increases autophagic flux and apoptosis after stress-induced p53 activation in cancer cells (Crighton *et al.*, 2006; Guan *et al.*, 2015).

Aneuploidy increases apoptosis in the trophectoderm and impairs the second lineage segregation in the inner cell mass

We further investigated if these effects are cell-type specific, as shown in the mouse (Bolton *et al.*, 2016; Singla *et al.*, 2020) and human 2D gastruloids (Yang *et al.*, 2021), and how they affect the first lineage segregation event to TE and ICM, and the second lineage segregation event to EPI and PrE.

We co-stained a new batch of expanded blastocysts (5dpf or 6dpf) for OCT4 (10 euploid, 14 aneuploid, ICM/EPI) and CASP3/7 (10 euploid, 14 aneuploid), LC3B (4 euploid, 5 aneuploid) or Serine 15 p53 (3 euploid, Aneuploid embryos showed a higher percentage of cells with activated p53 5 aneuploid) (Fig. 4a). All information on embryo score and developmental day and stage can be found in Supplementary Table 28. The latter marker was chosen to demonstrate that the transcriptomic signature of p53 signalling is caused by DNA-damage-induced phosphorylation of Serine-15 on p53 (Loughery *et al.*, 2014). Aneuploid embryos showed a higher percentage of cells with activated p53 (Fig. 4b,c), as suggested by our transcriptomic data (Figure 1), although these differences did not reach significance when considering the ICM/EPI (OCT4-positive) cells or TE (OCT4-negative) separately (Supplementary Fig. 2a-c). We then investigated cell type specificity of proliferative defects and apoptosis. Both the aneuploid TE and OCT4-positive cells showed decreased cell numbers (Fig. 4d-f) that led to an overall decrease of cell numbers in whole aneuploid embryos (Fig. 4g), confirming our previous experiment (Fig. 3g). The observed increased percentage of nuclear CASP3/7 positive cells in the TE of aneuploid embryos (Fig. 4h,i) and increased CASP3/7 mean intensity per cell in whole aneuploid embryos (Fig. 4h,j) points to apoptosis as the cause of this decrease in cell numbers. However, no OCT4-positive cells of either euploid or aneuploid group showed nuclear CASP3/7 signal (Fig. 4h). We also found CASP3/7-positive micronuclei which were increased in number in aneuploid embryos (Fig. 4h, Supplementary Fig. 2d,e).

The observation (figure 4f) that the ICM/EPI cell numbers of aneuploid embryos fell into two groups with either low or high cell counts led us to further investigate the impact of aneuploidies on the second lineage segregation event. All blastocysts were

re-stained for GATA4 (PrE marker) and imaged together with OCT4 (ICM/EPI marker). We found that while all euploid embryos contained GATA4-positive cells, 7/14 aneuploid embryos had no GATA4-positive cells (Fig. 4k,l). Further, in those seven aneuploid embryos with a GATA4-positive PrE cells, we observed a significantly lower PrE/EPI ratio (Fig. 4m). We then investigated whether there are different levels of LC3B as marker of autophagy between the aneuploid TE and ICM in an additional 5 aneuploid and 4 euploid embryos. Aneuploid embryos displayed increased levels of autophagy mainly attributable to the TE (Fig. 4n-q), while their ICM/EPI cells showed a small increase in autophagy which did not reach significance (Fig. 4q). The aneuploid embryos could be separated in two groups: a first group with low levels of autophagy lacking GATA4-positive cells in 2 out of 3 embryos (Fig. 4n, left and right panels, 2nd row) and a high-level autophagy group in which both embryos contained GATA4-positive cells (Fig. 4n, left and right panels 3rd row).

Lastly, we separated the aneuploid embryos into a low- and a high-dosage group as done for the gene-expression analysis (Supplementary Table 29). Trend analysis showed that the higher the number of imbalanced loci, the lower the cell numbers in the TE and PrE but not in the EPI (Fig. 4r).

Discussion

In this work, we studied the consequences of aneuploidy in human preimplantation embryos that carried a uniformly present, presumed meiotic, complex aneuploidy. We selected this type of genetic imbalances because we hypothesized that in the embryo, these would result into stronger and potentially different cellular stress responses than single meiotic aneuploidy or mosaic aneuploidy. In our study we find that, while aneuploid embryos had lower cell numbers in both TE and ICM/EPI, the effect of aneuploidy was cell-type dependent. Aneuploid TE presented transcriptomic signatures of p53 signalling and apoptosis, and immunostaining of whole embryos showed that aneuploidy results in increased proteotoxic stress, autophagy, DNA damage-mediated activated p53 and subsequent apoptosis in the TE. In contrast, aneuploidy impaired the second lineage differentiation, in particular PrE formation.

Overall, our gene-expression results are in line with previously published RNA-sequencing studies on aneuploid human embryonic cells that identified transcriptional signatures consistent with DNA damage (Vera-Rodriguez *et al.*, 2015; Licciardi *et al.*, 2018; Fuchs Weizman *et al.*, 2019), alteration of cell proliferation (Starostik *et al.*, 2020; Maxwell *et al.*, 2022), the cell cycle (Vera-Rodriguez *et al.*, 2015; Licciardi *et al.*, 2018; Fuchs Weizman *et al.*, 2019; Starostik *et al.*, 2020), deregulation of autophagy (Licciardi *et al.*, 2018; Sanchez-Ribas *et al.*, 2019), p53 signalling (Licciardi *et al.*, 2018) and apoptosis (Licciardi *et al.*, 2018; Groff *et al.*, 2019; Sanchez-Ribas *et al.*, 2019; Maxwell *et al.*, 2022). However, when comparing our dataset of differentially expressed genes to these studies, we only found modest overlaps at the level of individual genes. This is probably because embryos of different developmental stages were included in the studies, containing specific aneuploidies, and of different sample types (overview in Supplementary Table 17).

Naturally acquired and induced aneuploidies only share a few differentially expressed genes but show overall equal signatures after pathway analysis, suggesting that reversine-based models of aneuploidy are very close but may not fully mimic endogenous aneuploidy. We also observed aneuploidy-mediated gene dosage effects in the TE cells, as extensively reported in human and mouse aneuploid cancer cell lines (Dürrbaum and Storchová, 2016), and found that a higher dosage leads to stronger p53 signalling and apoptosis responses.

We next tested the predictions made based on the gene-expression profiles with immunostaining. First, we found evidence of proteotoxic stress and increased expression of autophagy proteins, as well as activation of apoptosis. The most likely series of events is that p62/LC3B/CASP8 interaction results in autophagy-mediated apoptosis in aneuploid human embryos. Nevertheless, we cannot rule out indirect activation of apoptosis mediated by autophagy due to the degradation of cell organelles (Gump and Thorburn, 2011). This is supported by the observation in the aneuploid mouse embryo model that autophagy is independent of the mTOR pathway (Singla *et al*., 2020). Other upstream regulators of autophagy could be involved, such as the cGAS-STING pathway (Krivega *et al.*, 2021) or, as also observed in our dataset, p53-mediated activation of DRAM1 (Crighton *et al.*, 2006) that can induce apoptosis by increasing BAX protein levels (Guan *et al.*, 2015). Second, we confirmed the presence of activated *p53* in aneuploid human embryos. We specifically stained for p53 with phosphorylation on Serine 15, mediated by kinases such as ATM and ATR as a direct result of DNA-damage (Loughery *et al*., 2014). This indicates that aneuploidy also induces the DNA-damage response in the embryo, as found in the mouse and 2D gastruloids (Singla *et al.*, 2020; Yang *et al.*, 2021). An interesting observation is that aneuploid embryos contained increased

numbers of CASP3/7 positive micronuclei. This is similar to findings in a non-human primate model showing that abnormal chromosomes can be encapsulated in micronuclei, which can subsequently be selectively eliminated from the embryo (Daughtry *et al.*, 2019). In human cleavage stage embryos these micronuclei have been shown to contain genetic material that originates from chromosome breakages due to replication fork stalling and DNA-damage (Palmerola *et al.*, 2022), further highlighting how aneuploidy is leading to DNA-damage in the human embryo. In sum, our results in this part are in line with previous findings on mouse and 2D gastruloid models, and suggest that at least two different stress responses are activated in fully aneuploid embryos with complex karyotypes, both converging on apoptosis if not resolved. First, proteotoxic stress resulting from gene-dosage imbalances mediates the unfolded protein response and autophagy. Second, DNA-damage mediates p53 activation that likely occurs due to replication stress as occurring in cancer and yeast (Santaguida and Amon, 2015; Zhu *et al.*, 2018).

In the second part of our work, we focused on studying the lineage-specific response to complex aneuploidy, as the studies on reversine-treated mouse embryos (Bolton *et al.*, 2016; Singla *et al.*, 2020) and human 2D gastruloids (Yang *et al.*, 2021) also identified a cell-type specific effect of aneuploidy. In the mouse, aneuploid cells are eliminated by apoptosis in the EPI, while tolerated in the TE, and in human 2D gastruloids, aneuploid cells are eliminated in the post-gastrulation embryonic germ layers but tolerated in the TE.

In our work, we used 5-6dpf human expanded blastocysts to study the consequences of aneuploidy on lineage segregation, identifying the ICM/EPI as staining positive for OCT4 and the PrE as positive for GATA4. We confirmed that the embryos analysed were expanded blastocysts which had undergone the first lineage segregations, as

OCT4 was restricted to the inner cells and absent in TE cells (Niakan and Eggan, 2013). The identity of human ICM and EPI cells is currently under vigorous debate (Meistermann *et al.*, 2021) and exclusive markers of either cell type are untested, therefore we cannot assign ICM or EPI identity to OCT4-positive cells. However, in blastocysts with GATA4-positive cells the second lineage segregation had occurred and PrE was established, and consequently we confidently assigned EPI identity to OCT4-positive cells in these blastocysts. Conversely, in GATA4-negative embryos OCT4-positive cells could be either ICM or EPI cells. Interestingly, we never found GATA4-positive cells in the absence of OCT4-positive cells, supporting the hypothesis that PrE cells differentiate from EPI cells (Meistermann *et al.*, 2021). While we detected lower cell numbers in aneuploid OCT4-positive ICM/EPI cells, they did not contain a single CASP3/7 positive cell. This difference with the mouse results is likely due to species-specific properties of the pluripotent cells: the lack of apoptosis in the human ICM/EPI could be due to an uncoupling between aneuploidy-induced stress signals and apoptosis, as observed in human and mouse pluripotent stem cells (Mantel *et al.*, 2007) . The lower cell numbers could be explained by two other known effects of *p53* activation. First, *p53* activation decreases cell proliferation, leading to lower cell numbers. Secondly, *p53* activation may downregulate *OCT4* and *NANOG* expression, as seen in mouse embryonic stem cells (Lin *et al.*, 2005), leading to loss of pluripotency and driving the cells to differentiation and out of the ICM/EPI. It is worth noting that our results are in contrast to findings of Victor et al, where both TE and ICM/EPI of mosaic and aneuploid embryos showed increased apoptosis (Victor *et al.*, 2019). Further work will be needed to understand if these discrepancies are due to technical or biological factors.

A second difference we observed was that the aneuploid TE had increased levels of autophagy markers, which did not reach statistical significance in the ICM/EPI. Interestingly, the aneuploid OCT4-positive results separated into a high and a low-level autophagy group, where the low-level group seemed to lack GATA4-positive PrE cells. Although based on a few samples, this data suggests that an ICM in a transcriptionally earlier state of pluripotency, i.e. GATA4-negative and prior to the second lineage segregation event, might be less sensitive to the consequences of aneuploidy, i.e. show less autophagy. We thus propose that aneuploid human embryonic cells in the ICM become more sensitive from the second lineage segregation onwards. We hypothesize that this effect may even become stronger and more specific to the embryonic lineage after onset of gastrulation, as elegantly shown in human 2D gastruloids (Yang *et al.*, 2021).

Finally, we found that in those embryos that had already undergone the second lineage segregation event, the aneuploid embryos had a significantly lower ratio of PrE to EPI cells than euploid embryos. Further, this effect was dosage-dependent, with embryos with larger gene-dosage imbalances showing significantly lower cell numbers in the TE and PrE than euploid embryos or embryos with lower gene-dosage imbalances. This suggests that complex aneuploidy both impairs TE/ICM proliferation and PrE formation or that the PrE is more sensitive to aneuploidy-mediated apoptosis than the less differentiated epiblast. Whether this effect is also driven by p53 activation remains to be confirmed.

Taken together, our results suggest that while the same pathways appear to be activated in human and mouse embryos with complex aneuploidy, human embryos have a different response when it comes to the downstream effect of these pathways in the different lineages. While the mouse readily depletes aneuploid cells by

apoptosis specifically from the embryonic lineage before implantation (Bolton *et al.*, 2016; Singla *et al.*, 2020), in the preimplantation human embryo, apoptosis appears to be more active in the TE. The results suggest that in the human embryo, undifferentiated pluripotent cells have a different response to aneuploidy-induced cellular stress than the neighbouring differentiated cells.

To conclude, our results on human embryos with complex meiotic aneuploidy provide further insight into the mechanisms by which human embryos respond to gene-dosage imbalances, and may contribute to understanding how aneuploid cells are selectively eliminated in mosaic embryos. Further research, especially by using human embryos with endogenous chromosomal mosaicism, will be needed to shed light on the interactions between proteotoxic stress, the p53 pathway and differentiation during early development, for which the most novel models of human embryo implantation (Deglincerti *et al.*, 2016; Shahbazi *et al.*, 2016, 2020; Kagawa *et al.*, 2021) will prove to be of incalculable value.

References

Banin S, Moyal L, Shieh SY, Taya Y, Anderson CW, Chessa L, Smorodinsky NI, Prives C, Reiss Y, Shiloh Y, *et al.* Enhanced phosphorylation of p53 by ATM in response to DNA damage. *Science* [Internet] 1998;**281**:1674–1677. Science.

Bolton H, Graham SJL, Aa N van der, Kumar P, Theunis K, Fernandez Gallardo E, Voet T, Zernicka-Goetz M. Mouse model of chromosome mosaicism reveals lineage-specific depletion of aneuploid cells and normal developmental potential. *Nat Commun* [Internet] 2016;**7**:1–12. Nature Publishing Group.

Capalbo A, Poli M, Rienzi L, Girardi L, Patassini C, Fabiani M, Cimadomo D, Benini F, Farcomeni A, Cuzzi J, *et al.* Mosaic human preimplantation embryos and their developmental potential in a prospective , non-selection clinical trial. Am. J. Hum. Genet., 108 (2021), pp. 2238-2247.

Capalbo A, Wright G, Elliott T, Ubaldi FM, Rienzi L, Nagy ZP. FISH reanalysis of inner cell mass and trophectoderm samples of previously array-CGH screened blastocysts shows high accuracy of diagnosis and no major diagnostic impact of mosaicism at the blastocyst stage. *Human Reproduction* 2013;**28**:2298–2307. Oxford University Press.

Chavez SL, Loewke KE, Han J, Moussavi F, Colls P, Munne S, Behr B, Reijo Pera RA. Dynamic blastomere behaviour reflects human embryo ploidy by the four-cell stage. *Nat Commun* [Internet] 2012;**3**:. Nat Commun.

Chow JFC, Yeung WSB, Lau EYL, Lee VCY, Ng EHY, Ho PC. Array comparative genomic hybridization analyses of all blastomeres of a cohort of embryos from young IVF patients revealed significant contribution of mitotic errors to embryo mosaicism at the cleavage stage. *Reprod Biol Endocrinol* [Internet] 2014;**12**:. Reprod Biol Endocrinol.

Coorens THH, Oliver TRW, Sanghvi R, Sovio U, Cook E, Vento-Tormo R, Haniffa M, Young MD, Rahbari R, Sebire N, *et al.* Inherent mosaicism and extensive mutation of human placentas. *Nature* 2021;**592**:80–85. Nature Research.

Crighton D, Wilkinson S, O'Prey J, Syed N, Smith P, Harrison PR, Gasco M, Garrone O, Crook T, Ryan KM. DRAM, a p53-Induced Modulator of Autophagy, Is Critical for Apoptosis. *Cell* 2006;**126**:121–134. Elsevier B.V.

Daughtry BL, Rosenkrantz JL, Lazar NH, Fei SS, Redmayne N, Torkenczy KA, Adey A, Yan M, Gao L, Park B, *et al.* Single-cell sequencing of primate preimplantation embryos reveals chromosome elimination via cellular fragmentation and blastomere exclusion. *Genome Res* [Internet] 2019;**29**:367–382. Cold Spring Harbor Laboratory Press.

David K Gardner, William B Schoolcraft. Culture and transfer of human blastocysts. *Curr Opin Obstet Gynecol* 1999;**11**:307–311.

Deglincerti A, Croft GF, Pietila LN, Zernicka-Goetz M, Siggia ED, Brivanlou AH. Self-organization of the in vitro attached human embryo. *Nature* [Internet] 2016;**533**:251–254.

Dobin A, Davis CA, Schlesinger F, Drenkow J, Zaleski C, Jha S, Batut P, Chaisson M, Gingeras TR. STAR: ultrafast universal RNA-seq aligner. *Bioinformatics* 2013;**29**:15–21.

Dürrbaum M, Kuznetsova A, Passerini V, Stingele S, Stoehr G, Storchová Z. Unique features of the transcriptional response to model aneuploidy in human cells. *BMC Genomics* [Internet] 2014;**15**:139. BioMed Central.

Dürrbaum M, Storchová Z. Effects of aneuploidy on gene expression: implications for cancer. *FEBS J* [Internet] 2016;**283**:791–802. John Wiley & Sons, Ltd.

Echten-Arends J van, Mastenbroek S, Sikkema-Raddatz B, Korevaar JC, Heineman MJ, Veen F van der, Repping S. Chromosomal mosaicism in human preimplantation embryos: a systematic review. *Hum Reprod Update* [Internet] 2011;**17**:620–627. Oxford University Press.

Fragouli E, Alfarawati S, Spath K, Babariya D, Tarozzi N, Borini A, Wells D. Analysis of implantation and ongoing pregnancy rates following the transfer of mosaic diploid–aneuploid blastocysts. *Hum Genet* [Internet] 2017;**136**:805–819. Springer Verlag.

Fragouli E, Munne S, Wells D. The cytogenetic constitution of human blastocysts: insights from comprehensive chromosome screening strategies. *Hum Reprod Update* [Internet] 2019;**25**:15–33. Oxford University Press.

Fuchs Weizman N, Wyse BA, Antes R, Ibarrientos Z, Sangaralingam M, Motamedi G, Kuznyetsov V, Madjunkova S, Librach CL. Towards Improving Embryo Prioritization: Parallel Next Generation Sequencing of DNA and RNA from a Single Trophectoderm Biopsy. *Sci Rep* [Internet] 2019;**9**:1–11. Nature Publishing Group.

Greco E, Minasi MG, Fiorentino F. Healthy Babies after Intrauterine Transfer of Mosaic Aneuploid Blastocysts. *New England Journal of Medicine* [Internet] 2015;**373**:2089–2090. Massachusetts Medical Society.

Griffin DK, Brezina PR, Tobler K, Zhao Y, Silvestri G, Mccoy RC, Anchan R, Benner A, Cutting GR, Kearns WG. The human embryonic genome is karyotypically complex, with chromosomally abnormal cells preferentially located away from the developing fetus. *Human Reproduction* [Internet] 2022; Oxford University Press (OUP).

Groff AF, Resetkova N, DiDomenico F, Sakkas D, Penzias A, Rinn JL, Eggan K. RNA-seq as a tool for evaluating human embryo competence. *Genome Res* [Internet] 2019;**29**:1705–1718. Cold Spring Harbor Laboratory Press.

Guan JJ, Zhang XD, Sun W, Qi L, Wu JC, Qin ZH. DRAM1 regulates apoptosis through increasing protein levels and lysosomal localization of BAX. *Cell Death Dis* [Internet] 2015;**6**:e1624–e1624. Nature Publishing Group.

Gump JM, Thorburn A. Autophagy and apoptosis: what is the connection? *Trends Cell Biol* [Internet] 2011;**21**:387–392. Trends Cell Biol.

Jacobs K, Velde H van de, Paepe C de, Sermon K, Spits C. Mitotic spindle disruption in human preimplantation embryos activates the spindle assembly checkpoint but not apoptosis until Day 5 of development. *MHR: Basic science of reproductive medicine* [Internet] 2017;**23**:321–329. Oxford University Press.

Jaiswal SK, Raj S, DePamphilis ML. Developmental Acquisition of p53 Functions. *Genes (Basel)* [Internet] 2021;**12**:1675. MDPI.

Johnson DS, Cinnioglu C, Ross R, Filby A, Gemelos G, Hill M, Ryan A, Smotrich D, Rabinowitz M, Murray MJ. Comprehensive analysis of karyotypic mosaicism between trophectoderm and inner cell mass. *MHR: Basic science of reproductive medicine* [Internet] 2010;**16**:944–949. Oxford University Press.

Kagawa H, Javali A, Khoei HH, Sommer TM, Sestini G, Novatchkova M, Scholte op Reimer Y, Castel G, Bruneau A, Maenhoudt N, *et al.* Human blastoids model blastocyst development and implantation. *Nature* [Internet] 2021;1–9. Nature Publishing Group

Kalousek DK, Vekemans M. Confined placental mosaicism. *J Med Genet* [Internet] 1996;**33**:529–533. BMJ Publishing Group.

Krivega M, Stiefel CM, Karbassi S, Andersen LL, Chunduri NK, Donnelly N, Pichlmair A, Storchová Z. Genotoxic stress in constitutive trisomies induces autophagy and the innate immune response via the cGAS-STING pathway. *Communications Biology 2021 4:1* [Internet] 2021;**4**:1–16. Nature Publishing Group.

Landuyt L Van, Stoop D, Verheyen G, Verpoest W, Camus M, Velde H Van De, Devroey P, Abbeel E Van Den. Outcome of closed blastocyst vitrification in relation to blastocyst quality: Evaluation of 759 warming cycles in a single-embryo transfer policy. *Human Reproduction* 2011;**26**:527–534. Oxford University Press.

Li B, Dewey CN. RSEM: accurate transcript quantification from RNA-Seq data with or without a reference genome. *BMC Bioinformatics* 2011;**12**:323.

Licciardi F, Lhakhang T, Kramer YG, Zhang Y, Heguy A, Tsirigos A. Human blastocysts of normal and abnormal karyotypes display distinct transcriptome profiles. *Sci Rep* [Internet] 2018;**8**:1–9. Nature Publishing Group.

Lin T, Chao C, Saito S, Mazur SJ, Murphy ME, Appella E, Xu Y. p53 induces differentiation of mouse embryonic stem cells by suppressing Nanog expression. *Nat Cell Biol* [Internet] 2005;**7**:165–171. Nat Cell Biol.

Loughery J, Cox M, Smith LM, Meek DW. Critical role for p53-serine 15 phosphorylation in stimulating transactivation at p53-responsive promoters. *Nucleic Acids Res* [Internet] 2014;**42**:7666–7680. Oxford University Press.

Love MI, Huber W, Anders S. Moderated estimation of fold change and dispersion for RNA-seq data with DESeq2. *Genome Biol* 2014;**15**:. BioMed Central Ltd.

Mantel C, Guo Y, Lee MR, Kim M-K, Han M-K, Shibayama H, Fukuda S, Yoder MC, Pelus LM, Kim K-S, *et al.* Checkpoint-apoptosis uncoupling in human and mouse embryonic stem cells: a source of karyotpic instability. *Blood* [Internet] 2007;**109**:4518–4527.

Maxwell SM, Lhakhang TC, Lin Z, Kramer YG, Zhang Y, Wang F, Heguy A, Tsirigos A, Grifo JA, Licciardi F. Investigation of Global Gene Expression of Human Blastocysts Diagnosed as Mosaic using Next-generation Sequencing. *Reproductive Sciences* [Internet] 2022;1–11.

McCoy RC. Mosaicism in Preimplantation Human Embryos: When Chromosomal Abnormalities Are the Norm. *Trends in Genetics* [Internet] 2017;**33**:448–463. Elsevier.

Meistermann D, Bruneau A, Loubersac S, Reignier A, Firmin J, François-Campion V, Kilens S, Lelièvre Y, Lammers J, Feyeux M, *et al.* Integrated pseudotime analysis of human pre-implantation embryo single-cell transcriptomes reveals the dynamics of lineage specification. *Cell Stem Cell* 2021;**28**:1625-1640.e6.

Mertzanidou A, Spits C, Nguyen HT, Velde H van de, Sermon K. Evolution of aneuploidy up to Day 4 of human preimplantation development. *Human Reproduction* [Internet] 2013a;**28**:1716–1724. Oxford University Press.

Mertzanidou A, Wilton L, Cheng J, Spits C, Vanneste E, Moreau Y, Vermeesch JR, Sermon K. Microarray analysis reveals abnormal chromosomal complements in over 70% of 14 normally developing human embryos. *Human Reproduction* [Internet] 2013b;**28**:256–264. Oxford University Press.

Munné S, Blazek J, Large M, Martinez-Ortiz PA, Nisson H, Liu E, Tarozzi N, Borini A, Becker A, Zhang J, *et al.* Detailed investigation into the cytogenetic constitution and pregnancy outcome of replacing mosaic blastocysts detected with the use of high-resolution next-generation sequencing. *Fertil Steril* [Internet] 2017;**108**:62-71.e8. Elsevier Inc.

Munné S, Nakajima ST, Najmabadi S, Sauer M v., Angle MJ, Rivas JL, Mendieta L v., MacAso TM, Sawarkar S, Nadal A, *et al.* First PGT-A using human in vivo blastocysts recovered by uterine lavage: Comparison with matched IVF embryo controls. *Human Reproduction* [Internet] 2020a;**35**:70–80. Oxford University Press.

Munné S, Spinella F, Grifo J, Zhang J, Beltran MP, Fragouli E, Fiorentino F. Clinical outcomes after the transfer of blastocysts characterized as mosaic by high resolution Next Generation Sequencing- further insights. *Eur J Med Genet* 2020b;**63**:103741. Elsevier Masson SAS.

Niakan KK, Eggan K. Analysis of human embryos from zygote to blastocyst reveals distinct gene expression patterns relative to the mouse. *Dev Biol* [Internet] 2013;**375**:54–64. Dev Biol.

Ohashi A, Ohori M, Iwai K, Nakayama Y, Nambu T, Morishita D, Kawamoto T, Miyamoto M, Hirayama T, Okaniwa M, *et al.* Aneuploidy generates proteotoxic stress and DNA damage concurrently with p53-mediated post-mitotic apoptosis in SAC-impaired cells. *Nat Commun* [Internet] 2015;**6**:1–16. Nature Publishing Group.

Oromendia AB, Dodgson SE, Amon A. Aneuploidy causes proteotoxic stress in yeast. *Genes Dev* 2012;**26**:2696–2708.

Orvieto R, Shimon C, Rienstein S, Jonish-Grossman A, Shani H, Aizer A. Do human embryos have the ability of self-correction? *Reprod Biol Endocrinol* [Internet] 2020;**18**:. Reprod Biol Endocrinol.

Palmerola KL, Amrane S, Los Angeles A de, Xu S, Wang N, Pinho J de, Zuccaro M v, Taglialatela A, Massey DJ, Turocy J, *et al.* Replication stress impairs chromosome segregation and preimplantation development in human embryos. *Cell* [Internet] 2022.

Pan J-A, Ullman E, Dou Z, Zong W-X. Inhibition of protein degradation induces apoptosis through a microtubule-associated protein 1 light chain 3-mediated activation of caspase-8 at intracellular membranes. *Mol Cell Biol* [Internet] 2011;**31**:3158–3170. American Society for Microbiology.

Popovic M, Dhaenens L, Boel A, Menten B, Heindryckx B. Chromosomal mosaicism in human blastocysts: The ultimate diagnostic dilemma. *Hum Reprod Update* [Internet] 2020;**26**:313–334. Oxford University Press.

Popovic M, Dheedene A, Christodoulou C, Taelman J, Dhaenens L, Nieuwerburgh F Van, Deforce D, Abbeel E Van Den, Sutter P De, Menten B, *et al.* Chromosomal mosaicism in human blastocysts: The ultimate challenge of preimplantation genetic testing? *Human Reproduction* [Internet] 2018;**33**:1342–1354. Oxford University Press.

Regin M, Spits C, Sermon K. On the origins and fate of chromosomal abnormalities in human preimplantation embryos: an unsolved riddle. *Mol Hum Reprod* [Internet] 2022; Mol Hum ReprodAvailable from: https://academic.oup.com/molehr/advance-article/doi/10.1093/molehr/gaac011/6566308.

Ren Y, Yan Z, Yang M, Keller L, Zhu X, Lian Y, Liu Q, Li R, Zhai F, Nie Y, *et al.* Regional and developmental characteristics of human embryo mosaicism revealed by single cell sequencing. *PLoS Genet* 2022;**18**:. Public Library of Science.

Ritchie ME, Phipson B, Wu D, Hu Y, Law CW, Shi W, Smyth GK. Limma powers differential expression analyses for RNA-sequencing and microarray studies. *Nucleic Acids Res* [Internet] 2015;**43**:e47. Oxford University Press.

Robinson MD, McCarthy DJ, Smyth GK. edgeR: A Bioconductor package for differential expression analysis of digital gene expression data. *Bioinformatics* 2009;**26**:139–140. Oxford University Press.

Robinson MD, Oshlack A. *A scaling normalization method for differential expression analysis of RNA-seq data* [Internet]. 2010.

Sanchez-Ribas I, Diaz-Gimeno P, Sebastián-León P, Mercader A, Quiñonero A, Ballesteros A, Pellicer A, Domínguez F. Transcriptomic behavior of genes associated with chromosome 21 aneuploidies in early embryo development. *Fertil Steril* 2019;**111**:991-1001.e2. Elsevier Inc.

Santaguida S, Amon A. Short- and long-term effects of chromosome mis-segregation and aneuploidy. *Nat Rev Mol Cell Biol* 2015;**16**:473–485.

Shahbazi MN, Jedrusik A, Vuoristo S, Recher G, Hupalowska A, Bolton V, Fogarty NME, Campbell A, Devito LG, Ilic D, *et al.* Self-organization of the human embryo in the absence of maternal tissues. *Nat Cell Biol* [Internet] 2016;**18**:700–708. Nature Publishing Group.

Shahbazi MN, Wang T, Tao X, Weatherbee BAT, Sun L, Zhan Y, Keller L, Smith GD, Pellicer A, Scott RT, *et al.* Developmental potential of aneuploid human embryos cultured beyond implantation. *Nat Commun* [Internet] 2020;**11**:1–15. Nature Research.

Singla S, Iwamoto-Stohl LK, Zhu M, Zernicka-Goetz M. Autophagy-mediated apoptosis eliminates aneuploid cells in a mouse model of chromosome mosaicism. *Nat Commun* [Internet] 2020;**11**:1–15. Nature Research.

Starostik MR, Sosin OA, McCoy RC. Single-cell analysis of human embryos reveals diverse patterns of aneuploidy and mosaicism. *Genome Res* 2020;**30**:814–826.

Stingele S, Stoehr G, Peplowska K, Cox J, Mann M, Storchova Z. Global analysis of genome, transcriptome and proteome reveals the response to aneuploidy in human cells. *Mol Syst Biol* [Internet] 2012;**8**:608. EMBO Press.

Vanneste E, Voet T, Caignec C le, Ampe M, Konings P, Melotte C, Debrock S, Amyere M, Vikkula M, Schuit F, *et al.* Chromosome instability is common in human cleavage-stage embryos. *Nat Med* [Internet] 2009;**15**:577–583. Nature Publishing Group.

Vázquez-Diez C, Paim LMG, FitzHarris G. Cell-Size-Independent Spindle Checkpoint Failure Underlies Chromosome Segregation Error in Mouse Embryos. *Current Biology* [Internet] 2019;**29**:865-873.e3. Cell Press.

Vera-Rodriguez M, Chavez SL, Rubio C, Pera RAR, Simon C. Prediction model for aneuploidy in early human embryo development revealed by single-cell analysis. *Nat Commun* [Internet] 2015;**6**:7601. Nature Publishing Group.

Victor AR, Tyndall JC, Brake AJ, Lepkowsky LT, Murphy AE, Griffin DK, McCoy RC, Barnes FL, Zouves CG, Viotti M. One hundred mosaic embryos transferred prospectively in a single clinic: exploring when and why they result in healthy pregnancies. *Fertil Steril* [Internet] 2019;**111**:280–293. Elsevier Inc.

Viotti M, Victor AR, Barnes FL, Zouves CG, Besser AG, Grifo JA, Cheng EH, Lee MS, Horcajadas JA, Corti L, *et al.* Using outcome data from one thousand mosaic embryo transfers to formulate an embryo ranking system for clinical use. *Fertil Steril* 2021;**115**:1212–1224. Elsevier Inc.

Voullaire L, Slater H, Williamson R, Wilton L. Chromosome analysis of blastomeres from human embryos by using comparative genomic hybridization. *Hum Genet* [Internet] 2000;**106**:210–217.

Wells D, Delhanty JD. Comprehensive chromosomal analysis of human preimplantation embryos using whole genome amplification and single cell comparative genomic hybridization. *Mol Hum Reprod* [Internet] 2000;**6**:1055–1062.

Yan L, Yang M, Guo H, Yang L, Wu J, Li R, Liu P, Lian Y, Zheng X, Yan J, *et al.* Single-cell RNA-Seq profiling of human preimplantation embryos and embryonic stem cells. *Nat Struct Mol Biol* [Internet] 2013;**20**:1131–1139. Nature Publishing Group.

Yang M, Rito T, Metzger J, Naftaly J, Soman R, Hu J, Albertini DF, Barad DH, Brivanlou AH, Gleicher N. Depletion of aneuploid cells in human embryos and gastruloids. *Nat Cell Biol* [Internet] 2021;**23**:314–321. Nature Research.

Zamani Esteki M, Viltrop T, Tšuiko O, Tiirats A, Koel M, Nõukas M, Žilina O, Teearu K, Marjonen H, Kahila H, *et al.* In vitro fertilization does not increase the incidence of de novo copy number alterations in fetal and placental lineages. *Nat Med* 2019;

Zhu J, Tsai HJ, Gordon MR, Li R. Cellular Stress Associated with Aneuploidy. *Dev Cell* [Internet] 2018;**44**:420–431. Cell Press.

Data availability

Data are available from the corresponding author upon reasonable request.

Acknowledgements

The authors would like to thank Marleen Carlé from the Center for Medical Genetics (UZ Brussel) for assisting during the tubing of trophectoderm samples. We thank Wilfried Cools from the Biostatistics and Medical Informatics Group (VUB) for the statistical advice and the members of the BRIGHTcore facility (UZ Brussel) for performing the RNA sequencing. We thank Prof. Rajiv McCoy for the scientific input and data exchange. This study was funded by the Fonds for Scientific Research in Flanders -G017218N- (Fonds Wetenschappelijk Onderzoek – Vlaanderen [FWO]). M.R. and E.C.D.D. are doctoral fellows at the FWO.

Author contributions

M.R. carried out all the experiments unless stated otherwise, interpreted and analyzed the results and co-wrote the manuscript. Y.L. and E.C.D.D. performed the bioinformatics analysis. Y.G. performed the trophectoderm biopsies. P.V. provided and supervised the diagnoses of the PGT embryos. G.V. and H.V.D.V. provided the embryos for this study. K.S. interpreted and supervised the experimental work and co-wrote the manuscript. C.S. designed, interpreted and supervised the experimental work and co-wrote the manuscript. All co-authors proofread the manuscript.

Competing interests

The authors declare no competing interests.

Fig. 1: RNA-sequencing of trophectoderm cells reveals deregulation of DNA damage, p53, cell-cycle, autophagy and apoptosis pathways in chromosomally abnormal human embryos.

a. Human blastocysts 5 or 6 days post-fertilization (dpf) underwent Preimplantation Genetic Testing (PGT) for monogenic diseases and/or aneuploidy screening, followed by cryopreservation. Embryos that were not transferred were donated for research after written informed content. After warming and 2hrs recuperation, euploid and fully aneuploid research embryos underwent a second TE biopsy for RNA-sequencing. The remainder of the embryos was live-stained with either CASP3/7 or CASP8 for 30min and fixed for immunostaining for proteins of interest (see figure 3). **b**. 3dpf human embryos were warmed and treated with 0.5µM reversine for 24hrs then transferred to normal culture medium until 5dpf to undergo TE biopsy for RNA-sequencing. After 2hrs recuperation the embryos were live-stained with CASP8 for 30min and fixed for immunostaining for proteins of interest (see figure 3). **c**. Unsupervised hierarchical clustering of all coding genes. Color coding: beige = euploid, red = aneuploid and blue = reversine-treated. **d**. Comparison between the diagnosis of aneuploid embryos obtained after PGT (list on the left) and the results obtained after using InferCNV after RNA-sequencing (plot on the right). **e**,**f**. Volcano plots after differential gene expression analysis with a cutoff value of $|\log_2$ fold change$| > 1$ and $-\log_{10}$(p-value) < 0.05 for aneuploid versus euploid (**e**) and reversine versus euploid (**f**). **g**,**h**. Venn diagrams comparing the upregulated (**g**) and downregulated (**h**) genes in aneuploid versus reversine treated embryos. **i**,**j**. Supervised plot of pathway analysis using the Molecular Signatures Database (FDR < 0.05) based on the list of all differentially expressed genes between aneuploid or reversine versus euploid embryos. Pathways are ranked based on the total number

of genes in overlap of both test sets, ranked from sets with the highest number of genes in overlap to sets with the lowest. Outputs of the Hallmark library and C5 ontology gene sets are shown in (**i**) and (**j**), respectively. **k**,**l**. Supervised plots after Ingenuity Pathway Analysis of upstream regulators with an activation z-score ≤ -2 and ≥ 2 and a p-value < 0.05 in the aneuploid (**k**) or reversine (**l**) versus euploid embryos. **m**,**n**. Supervised plots after Ingenuity Pathway Analysis of canonical pathways in aneuploid (**m**) or reversine (**n**) versus euploid embryos. Pathways are ranked by p-value from the most to the least significant, those with a p-value < 0.05 and with an activation z-score ≤ -1.5 and ≥ 1.5 were considered as inhibited or activated, respectively. Significant pathways with an activation z-score between -1.5 and 1.5 were considered as deregulated.

Fig. 2: Human embryos with the highest number of genes with abnormal copy number show stronger p53 pathway and apoptosis response.

a. Supervised hierarchical clustering of the TOP 500 deregulated genes sorted by p-value. Color coding: blue = euploid , green = Low dosage and red = High dosage. **b**,**c**. Volcano plots after differential gene expression analysis with a cutoff value of $|\log_2$ fold change$|$ > 1 and $-\log_{10}$(p-value) < 0.05 for low dosage versus euploid embryos (**b**) and high dosage versus euploid embryos (**c**). **d**,**e**, Venn diagrams comparing the upregulated (**d**) and downregulated (**e**) genes in low dosage versus high dosage embryos. **f**. Supervised plot of pathway analysis using the Hallmark library of the Molecular Signatures Database (FDR < 0.05) based on the list of the TOP 500 expressed genes by p-value between low or high dosage versus euploid embryos. Pathways are ranked based on FDR-q-values of both test sets, the most

significant deregulated pathway ranked from top to least significant pathway. **g**,**h**. Dot plots of the genes in overlap with the Hallmark p53 pathway (**g**) and Hallmark apoptosis pathway (**h**) of both low and high dosage embryos sorted by $\log_2$ Fold Change from the highest to the lowest. Dots with an increased size and a darker blue represent a higher value of $\log_2$ Fold Change and lower p-value, respectively. **i**, Violin plots with box and whisker plots of the counts per million mapped reads of a supervised set of 10 genes (from Supplementary Table 2) that are part of apoptosis (*BAD, BCL2L1, TNFRSF10B*), p53 pathway (*DRAM1, MDM2, CDKN1A/B, PURPL*), growth arrest (*GADD45A*), and DNA-damage (*DDB2*). *p = 0.027, **p = 0.010, ***p = 0.004, ****p < 0.001 using the Jonkheere-Terpstra test. Box and whisker plots show median and minimum to maximum values.

Fig. 3: Immunostaining reveals increased apoptosis, autophagy, proteotoxic stress and DNA-damage in chromosomally abnormal human embryos.

a,**b**. Same experimental set-up as described in **Fig. 1 a**,**b**, but focused on immunostaining analysis. **c**, Orthogonal projections after immunostaining of euploid and aneuploid embryos for DNA (white) and CASP3/7 (green). **d**, Orthogonal projections after immunostaining of euploid, aneuploid and reversine-treated embryos for DNA (white) and CASP8 (green). **e**, CASP3/7 mean intensity per cell. Euploid n=13, Aneuploid n=8 embryos. Mann-Whitney test, *p = 0.0199. **f**, CASP8 mean intensity per cell. Euploid n=6, Aneuploid n=9, Reversine-treated n=8 embryos. Kruskal-Wallis test, *p = 0.0394, **p = 0.0085. **g**, Number of nuclei per embryo. Euploid n=19, Aneuploid n=18, Reversine-treated n=8 embryos. Kruskal-Wallis test, ****p < 0.0001, *p = 0.0305. **h**, Orthogonal projections after immunostaining of euploid, aneuploid and reversine-treated embryos for DNA (white), LC3B (turquoise) and HSP70 (magenta). **i**, LC3B puncta per cell. Euploid n=19, Aneuploid n=22

embryos, Reversine-treated n=8 embryos. Kruskal-Wallis test, *p = 0.0189, **p = 0.0074. **j**, HSP70 mean intensity per cell. Euploid n=13, Aneuploid n=8, Reversine-treated n=8 embryos. Kruskal-Wallis test, **p = 0.0077, ***p = 0.0008. **k**, Orthogonal projections after immunostaining of euploid, aneuploid for DNA (white) and p62 (turquoise). **l**, p62 puncta per cell. Euploid n=6, Aneuploid n=9 embryos. Mann-Whitney test, **p = 0.0076.

Brightfield pictures were obtained during confocal imaging. All scale bars are 20 µm. Box and whisker plots show median and whiskers show minimum to maximum values. Bar plots show mean ± s.d. For all plots each dot represents a single embryo and ns = not significant.

Fig. 4: Aneuploid human embryos show less cells in trophectoderm and OCT4-positive cells and impaired primarily primitive endoderm differentiation

a, 5 or 6dpf post-PGT-A euploid and fully aneuploid human blastocysts were warmed and kept for 16hrs in culture to allow for the second lineage segregation. The blastocysts were live-stained with CASP3/7 for 30min and fixed for immunostaining proteins of interest. In a first scan we analyzed OCT4 (ICM), CASP3/7 (apoptosis), LC3B (autophagy) and S15p53 (DNA damage) in both lineages. Embryos were then re-stained with GATA4 as a marker for PrE. **b,** Orthogonal projections after immunostaining of euploid, aneuploid for DNA (white) and Serine (S) 15 p53 (turquoise). **c**, Percentage (%) of Serine 15 p53 positive cells per embryo. Euploid n = 3, Aneuploid n = 5. Mann-Whitney test, *p = 0.0357. **d**, Orthogonal projections after immunostaining of euploid and aneuploid embryos for DNA (white) and OCT4 (magenta). The first aneuploid panel (Trisomy 14 and 16) shows a similar number of

ICM cells compared to the euploid embryo. The second aneuploid panel (Trisomy 14 and 22) shows an embryo without an ICM. **e,f**,**g**, Differences in number of nuclei per embryo between euploid and aneuploid embryos in the OCT4-negative cells (trophectoderm) (**e**) **p = 0.0092 , OCT4-positive cells (ICM/EPI), *p = 0.0412 (**f**) and whole embryo **p = 0.0067 (**g**). Euploid n = 10, Aneuploid n = 14. Student's t-test with Welch's correction**.** **h**, Orthogonal projections after immunostaining of euploid and aneuploid embryos for DNA (white), CASP3/7 (green) and OCT4 (magenta). **i**, Percentage (%) of CASP3/7 positive (+) cells in the trophectoderm lineage (OCT4-negative cells). Euploid n = 9, Aneuploid n = 14. Student's t-test with Welch's correction, *p = 0.0453. **j**, CASP3/7 mean intensity per cell of whole embryos. Euploid n = 9, Aneuploid n = 14. Student's t-test with Welch's correction, *p = 0.0332. **k**, Orthogonal projections after immunostaining of euploid and aneuploid embryos for DNA (white), OCT4 (magenta) and GATA4 (green). The first aneuploid panel (trisomy 13 and 15) shows an embryo with presence of a GATA4 positive cell (PrE). The second aneuploid panel (Trisomy 7 and monosomies 5, 12 and 21) shows an embryo that did not contain GATA4 positive cells. **l**, Differences in the number of cells per embryo that were OCT4 positive and either GATA4 negative (red) or positive (green) between euploid and aneuploid embryos. In case GATA4-positive cells (PrE) were present we considered the GATA4-negative cells to be epiblast (EPI). All euploid embryos contained GATA4-positive cells, 7/14 aneuploid embryos had an ICM completely lacking GATA4-positive cells (Fisher-exact test, p = 0.0188). **m**, Differences in the PrE/EPI ratio between euploid and aneuploid embryos that had an ICM containing GATA4-positive cells. Euploid n = 9, Aneuploid n = 7. Note here that one euploid embryo (#6, **l**) was lost during re-staining for GATA4. Mann-Whitney test, **p = 0.0089. **n**, Orthogonal projections after immunostaining of euploid and aneuploid embryos for DNA (white), LC3B (turquoise) and OCT4 (magenta). Yellow

circle indicates the ICM. The first aneuploid panel (Trisomy 1 and 20 and monosomy 18) shows OCT4-positive cells (ICM/EPI) with low levels of autophagy and, after re-staining for GATA4, without PrE (right panel, ICM zoom). The second aneuploid panel (Monosomy 14) shows an embryo with high levels of autophagy in the ICM that contains PrE cells (right panel, ICM zoom). **o,p,q.** Differences in LC3B puncta per cell between euploid and aneuploid embryos in the whole embryo,*p = 0.0317 (**o**),(OCT4-negative cells (trophectoderm),*p = 0.0317 (**p**) and OCT4-positive cells (ICM/EPI) (**q**). Euploid n = 4, Aneuploid n = 5. Mann-Whitney test. **r**, Violin plots with box plots of OCT4-positive-cells (ICM/EPI) per embryo (left, ns), OCT4-negative cells (trophectoderm) per embryo (center, *p = 0.043) and GATA4-positive-cells (PrE) per embryo (right, ****p < 0.001, Jonkheere-Terpstra test) depending on gene dosage. Euploid (light blue), Low dosage (middle blue) and High dosage (darkest blue).

Yellow arrows indicate presence of the signal and yellow arrow heads indicate absence of signal. Brightfield pictures were obtained during confocal imaging. All scale bars are 20 µm. Box and whisker plots show median and minimum to maximum values. Bar plots show mean ± s.d. For all plots each dot represents a single embryo; ns = not significant. T = Trisomy, M = Monosomy

Supplementary Fig. 1: Expanded RNA-sequencing analysis

a, Principal component analysis after RNA-sequencing of euploid (green) versus aneuploid (red) and reversine (blue) embryos. **b**, InferCNV analysis of individual euploid samples compared to the reference set. **c**, InferCNV analysis of individual reversine samples compared to the reference set. **d**, Venn Diagram of overlap between differentially expressed genes of this study with two studies that analyzed

cleavage stage embryos that contain euploid and diverse types of aneuploidy from cleavage stage embryos (Vera-Rodriguez et al. 2015) and single cells from 4 and 7 dpf human embryos from TE, ICM, EPI and PrE lineages (Starostik et al. 2020). **e**, Venn Diagram of overlap between differentially expressed genes of this study with four studies that analyzed specific aneuploidies (Licciardi et al. 2018, Fuchs-Weizman et al. 2019, Sánchez-Ribas et al. 2019 and Maxwell et al. 2022).

Supplementary Fig. 2: S15-p53 expression in TE vs OCT4-positive cells (ICM/EPI) and increased micronuclei in aneuploid embryos

a, Orthogonal projections after immunostaining of euploid and aneuploid embryos for DNA (white), S15p53 (turquoise) and OCT4 (magenta). **b**, Percentages of nuclei positive for S15p53 per embryo in euploid (n = 3) and aneuploid (n = 4) embryos in the ICM. **c**, Percentages of nuclei positive for S15p53 per embryo in euploid (n = 3) and aneuploid (n = 5) embryos in the TE. **d**, Left panel: Orthogonal projections after immunostaining of euploid and aneuploid embryos for DNA (white) and CASP3/7 (green) showing micronuclei. Yellow box indicates zoomed-in region in the right panel. Yellow arrows indicate presence of micronuclei and overlap between DNA and CASP3/7. **e**, Number of micronuclei per cell in euploid and aneuploid whole embryos. Euploid n = 9, Aneuploid n = 14. Student's t-test with Welch's correction, *p = 0.0115.

Brightfield pictures were obtained during confocal imaging. All scale bars are 20 µm. Box and plots show median and minimum to maximum values. Bar plots show mean ± s.d. For all plots each dot represents a single embryo; ns = not significant. ROI = Region of interest.

1143

1144

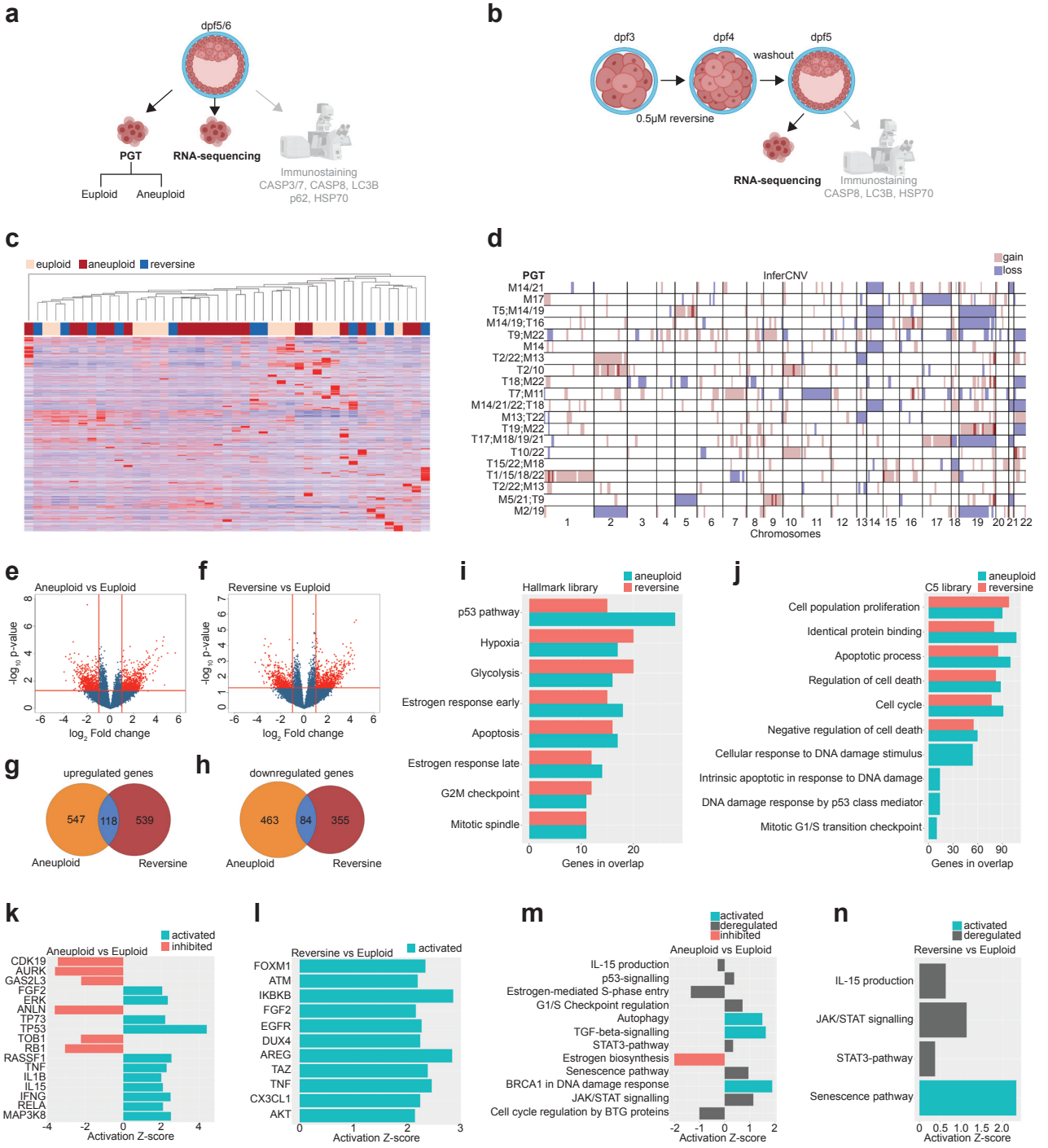
a
dpf5/6
PGT
RNA-sequencing
Euploid
Aneuploid
Immunostaining
CASP3/7, CASP8, LC3B
p62, HSP70
b
dpf3
dpf4
dpf5
washout
0.5μM reversine
RNA-sequencing
Immunostaining
CASP8, LC3B, HSP70
c
euploid
aneuploid
reversine
d
PGT
InferCNV
gain
loss
Chromosomes
e
Aneuploid vs Euploid
-log10 p-value
log2 Fold change
f
Reversine vs Euploid
-log10 p-value
log2 Fold change
g
upregulated genes
547
118
539
Aneuploid
Reversine
h
downregulated genes
463
84
355
Aneuploid
Reversine
i
Hallmark library
aneuploid
reversine
p53 pathway
Hypoxia
Glycolysis
Estrogen response early
Apoptosis
Estrogen response late
G2M checkpoint
Mitotic spindle
Genes in overlap
j
C5 library
aneuploid
reversine
Cell population proliferation
Identical protein binding
Apoptotic process
Regulation of cell death
Cell cycle
Negative regulation of cell death
Cellular response to DNA damage stimulus
Intrinsic apoptotic in response to DNA damage
DNA damage response by p53 class mediator
Mitotic G1/S transition checkpoint
Genes in overlap
k
Aneuploid vs Euploid
activated
inhibited
CDK19
AURK
GAS2L3
FGF2
ERK
ANLN
TP73
TP53
TOB1
RB1
RASSF1
TNF
IL1B
IL15
IFNG
RELA
MAP3K8
Activation Z-score
l
Reversine vs Euploid
activated
FOXM1
ATM
IKBKB
FGF2
EGFR
DUX4
AREG
TAZ
TNF
CX3CL1
AKT
Activation Z-score
m
activated
deregulated
inhibited
Aneuploid vs Euploid
IL-15 production
p53-signalling
Estrogen-mediated S-phase entry
G1/S Checkpoint regulation
Autophagy
TGF-beta-signalling
STAT3-pathway
Estrogen biosynthesis
Senescence pathway
BRCA1 in DNA damage response
JAK/STAT signalling
Cell cycle regulation by BTG proteins
Activation Z-score
n
activated
deregulated
Reversine vs Euploid
IL-15 production
JAK/STAT signalling
STAT3-pathway
Senescence pathway
Activation Z-score

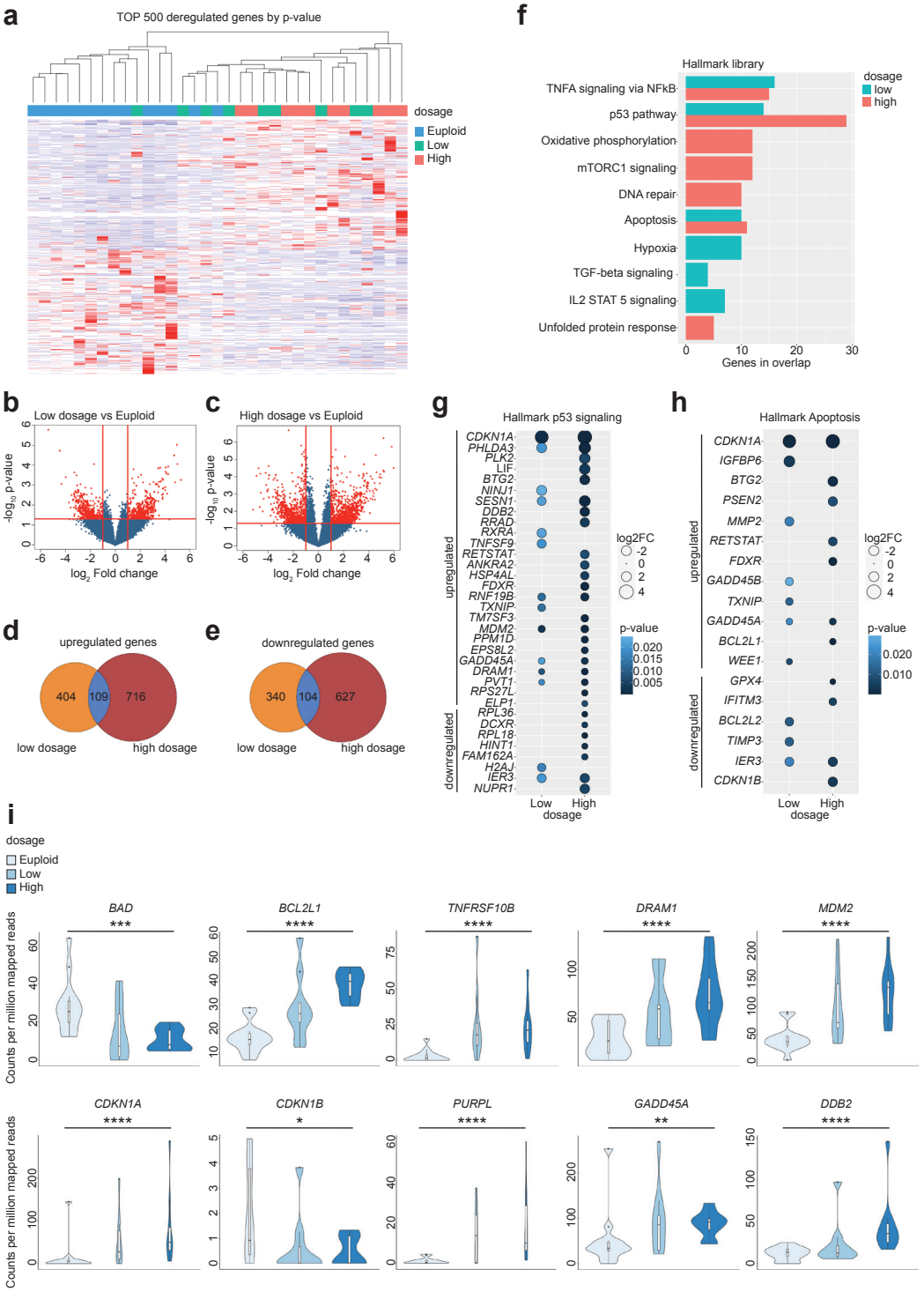
a
TOP 500 deregulated genes by p-value
dosage
Euploid
Low
High
f
Hallmark library
TNFA signaling via NFkB
p53 pathway
Oxidative phosphorylation
mTORC1 signaling
DNA repair
Apoptosis
Hypoxia
TGF-beta signaling
IL2 STAT 5 signaling
Unfolded protein response
Genes in overlap
dosage
low
high
b
Low dosage vs Euploid
-log10 p-value
log2 Fold change
c
High dosage vs Euploid
d
upregulated genes
404
109
716
low dosage
high dosage
e
downregulated genes
340
104
627
low dosage
high dosage
g
Hallmark p53 signaling
upregulated
downregulated
CDKN1A
PHLDA3
PLK2
LIF
BTG2
NINJ1
SESN1
DDB2
RRAD
RXRA
TNFSF9
RETSTAT
ANKRA2
HSP4AL
FDXR
RNF19B
TXNIP
TM7SF3
MDM2
PPM1D
EPS8L2
GADD45A
DRAM1
PVT1
RPS27L
ELP1
RPL36
DCXR
RPL18
HINT1
FAM162A
H2AJ
IER3
NUPR1
Low
High
dosage
log2FC
-2
0
2
4
p-value
0.020
0.015
0.010
0.005
h
Hallmark Apoptosis
upregulated
downregulated
CDKN1A
IGFBP6
BTG2
PSEN2
MMP2
RETSTAT
FDXR
GADD45B
TXNIP
GADD45A
BCL2L1
WEE1
GPX4
IFITM3
BCL2L2
TIMP3
IER3
CDKN1B
Low
High
dosage
log2FC
-2
0
2
4
p-value
0.020
0.010
i
dosage
Euploid
Low
High
BAD
BCL2L1
TNFRSF10B
DRAM1
MDM2
CDKN1A
CDKN1B
PURPL
GADD45A
DDB2
Counts per million mapped reads

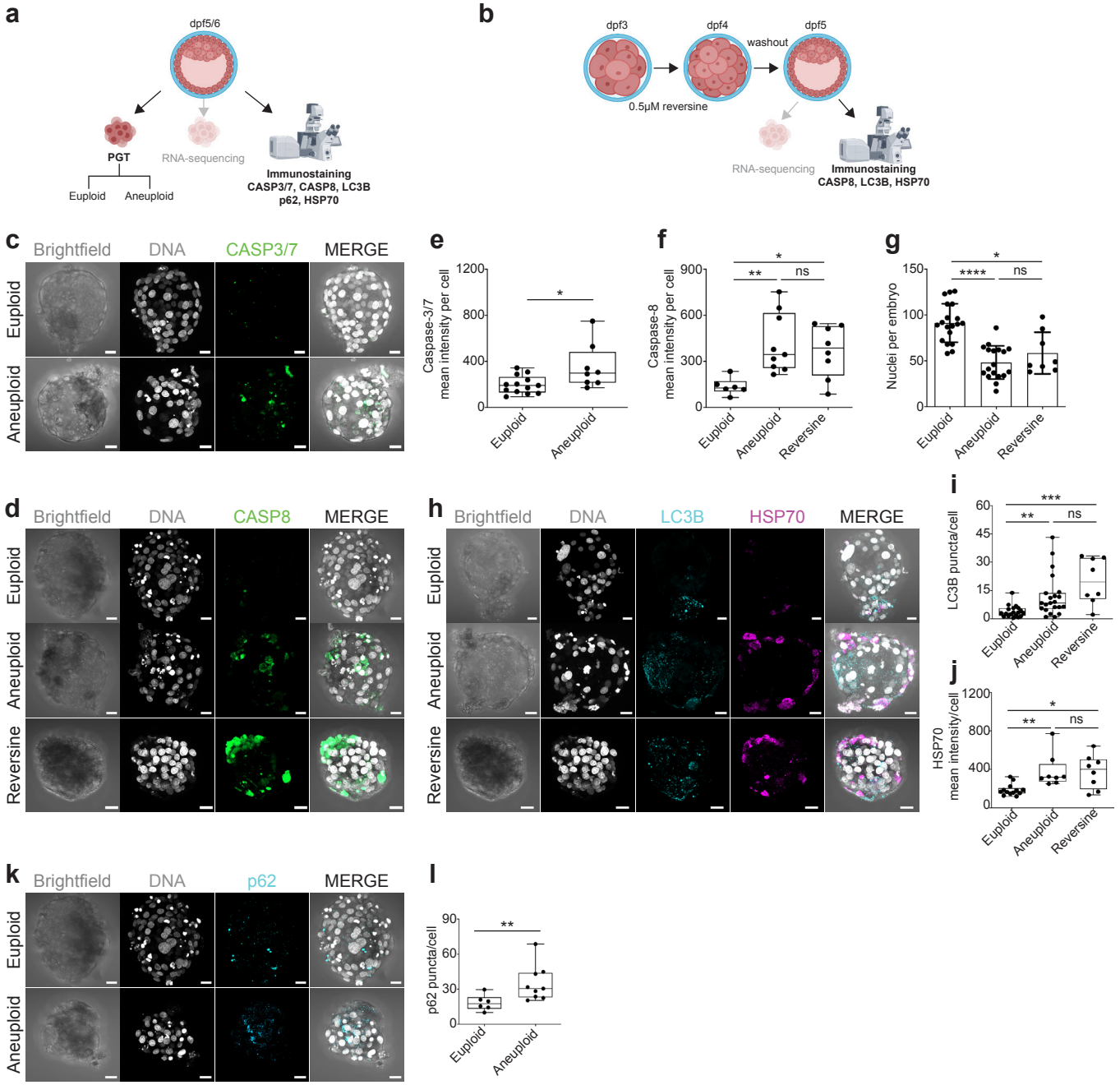
a
dpf5/6
PGT
RNA-sequencing
Euploid
Aneuploid
Immunostaining
CASP3/7, CASP8, LC3B
p62, HSP70
b
dpf3
dpf4
dpf5
washout
0.5μM reversine
RNA-sequencing
Immunostaining
CASP8, LC3B, HSP70
c
Brightfield
DNA
CASP3/7
MERGE
Euploid
Aneuploid
e
Caspase-3/7
mean intensity per cell
Euploid
Aneuploid
f
Caspase-8
mean intensity per cell
Euploid
Aneuploid
Reversine
g
Nuclei per embryo
Euploid
Aneuploid
Reversine
d
Brightfield
DNA
CASP8
MERGE
Euploid
Aneuploid
Reversine
h
Brightfield
DNA
LC3B
HSP70
MERGE
Euploid
Aneuploid
Reversine
i
LC3B puncta/cell
Euploid
Aneuploid
Reversine
j
HSP70
mean intensity/cell
Euploid
Aneuploid
Reversine
k
Brightfield
DNA
p62
MERGE
Euploid
Aneuploid
l
p62 puncta/cell
Euploid
Aneuploid

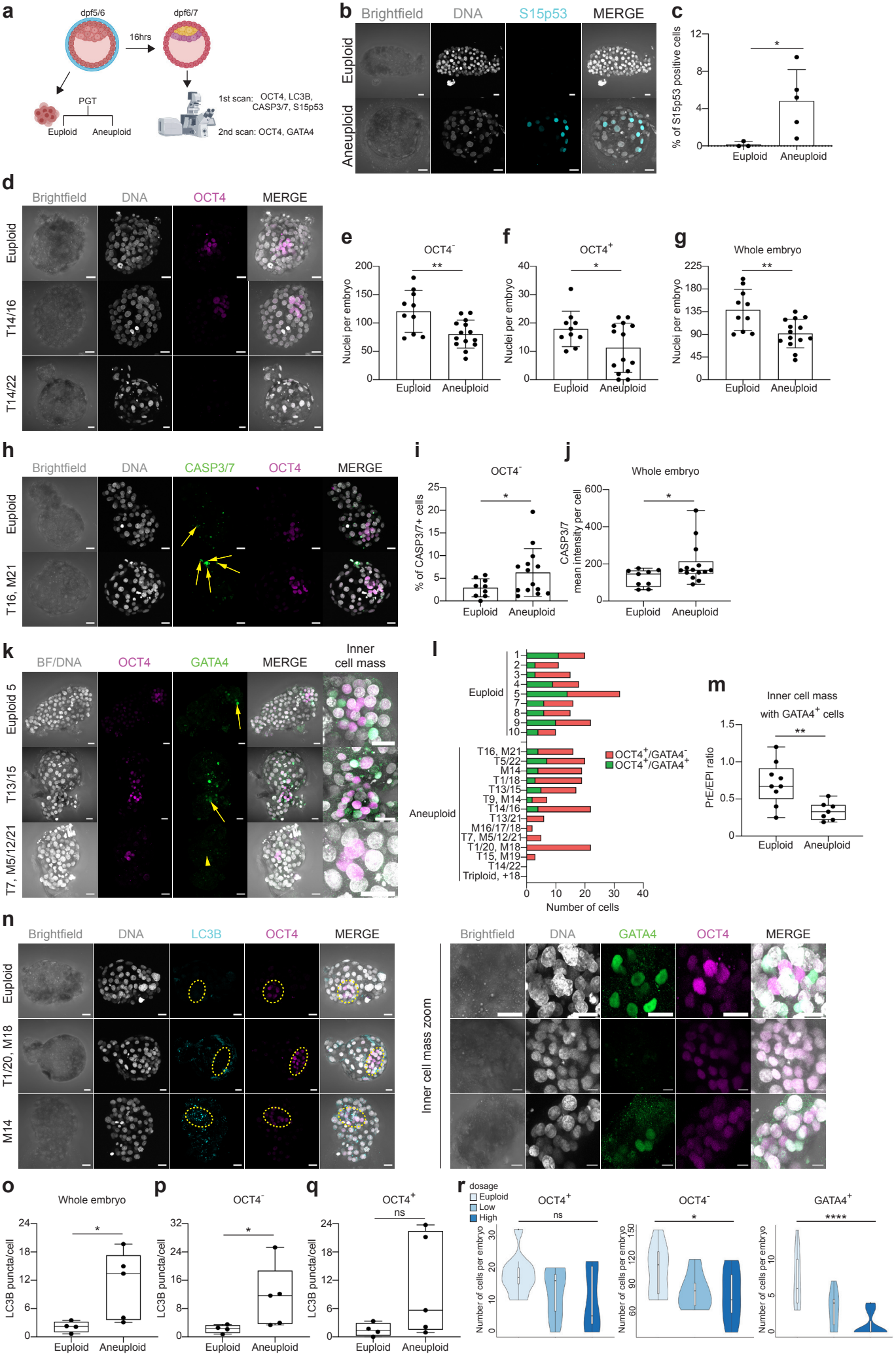
a
dpf5/6
16hrs
dpf6/7
PGT
Euploid
Aneuploid
1st scan: OCT4, LC3B, CASP3/7, S15p53
2nd scan: OCT4, GATA4
b
Brightfield
DNA
S15p53
MERGE
Euploid
Aneuploid
c
% of S15p53 positive cells
Euploid
Aneuploid
d
Brightfield
DNA
OCT4
MERGE
Euploid
T14/16
T14/22
e
OCT4-
Nuclei per embryo
Euploid
Aneuploid
f
OCT4+
Nuclei per embryo
Euploid
Aneuploid
g
Whole embryo
Nuclei per embryo
Euploid
Aneuploid
h
Brightfield
DNA
CASP3/7
OCT4
MERGE
Euploid
T16, M21
i
OCT4-
% of CASP3/7+ cells
Euploid
Aneuploid
j
Whole embryo
CASP3/7 mean intensity per cell
Euploid
Aneuploid
k
BF/DNA
OCT4
GATA4
MERGE
Inner cell mass
Euploid 5
T13/15
T7, M5/12/21
l
Euploid
Aneuploid
T16, M21
T5/22
M14
T1/18
T13/15
T9, M14
T14/16
T13/21
M16/17/18
T7, M5/12/21
T1/20, M18
T15, M19
T14/22
Triploid, +18
OCT4+/GATA4-
OCT4+/GATA4+
Number of cells
m
Inner cell mass with GATA4+ cells
PrE/EPI ratio
Euploid
Aneuploid
n
Brightfield
DNA
LC3B
OCT4
MERGE
Euploid
T1/20, M18
M14
Inner cell mass zoom
GATA4
o
Whole embryo
LC3B puncta/cell
Euploid
Aneuploid
p
OCT4-
LC3B puncta/cell
Euploid
Aneuploid
q
OCT4+
ns
LC3B puncta/cell
Euploid
Aneuploid
r
dosage
Euploid
Low
High
OCT4+
ns
OCT4-
GATA4+
Number of cells per embryo

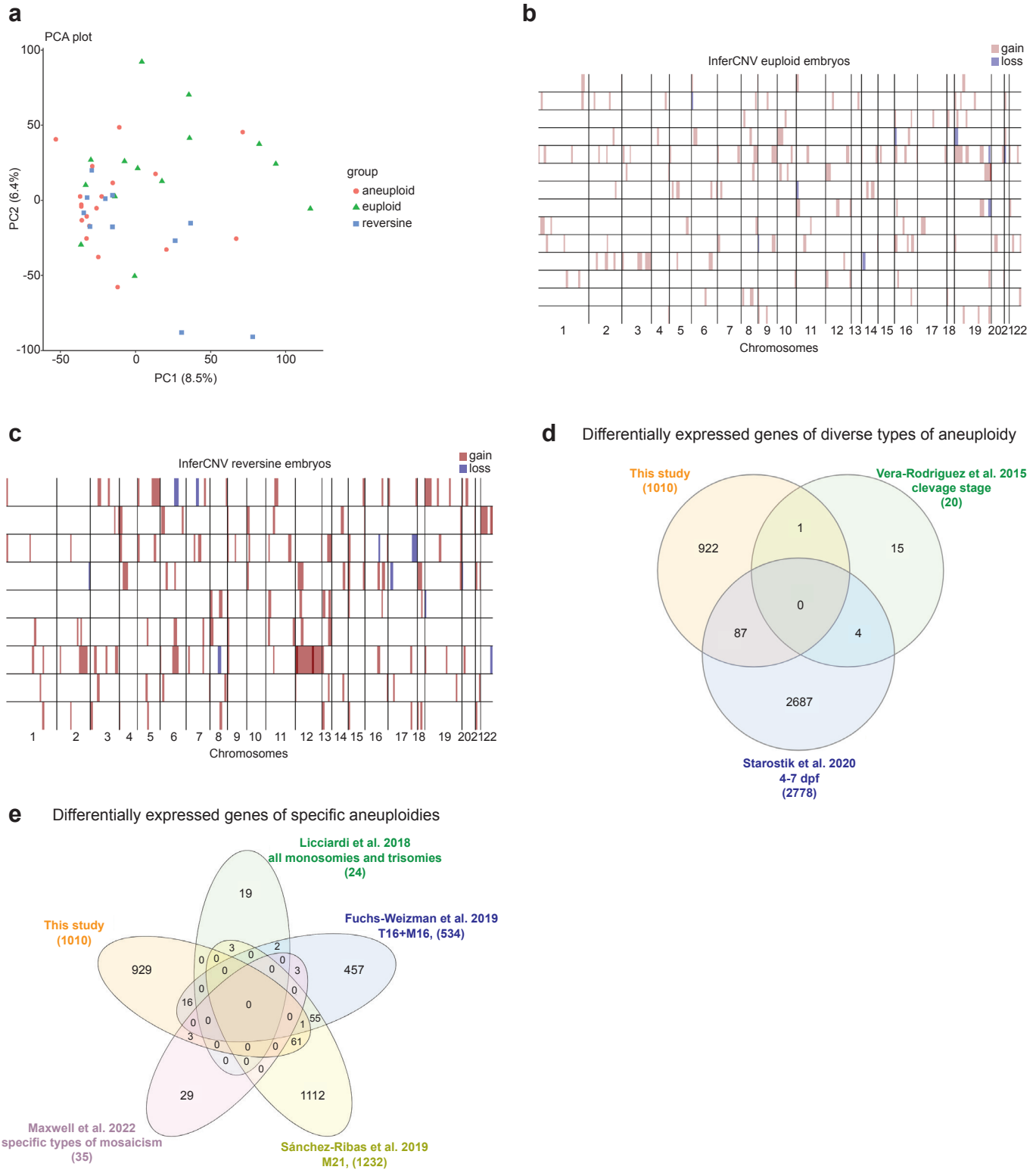
a
PCA plot
PC2 (6.4%)
PC1 (8.5%)
group
aneuploid
euploid
reversine
b
InferCNV euploid embryos
gain
loss
Chromosomes
c
InferCNV reversine embryos
gain
loss
Chromosomes
d
Differentially expressed genes of diverse types of aneuploidy
This study (1010)
Vera-Rodriguez et al. 2015 clevage stage (20)
Starostik et al. 2020 4-7 dpf (2778)
922
1
15
0
87
4
2687
e
Differentially expressed genes of specific aneuploidies
Licciardi et al. 2018 all monosomies and trisomies (24)
This study (1010)
Fuchs-Weizman et al. 2019 T16+M16, (534)
Maxwell et al. 2022 specific types of mosaicism (35)
Sánchez-Ribas et al. 2019 M21, (1232)
19
929
457
29
1112

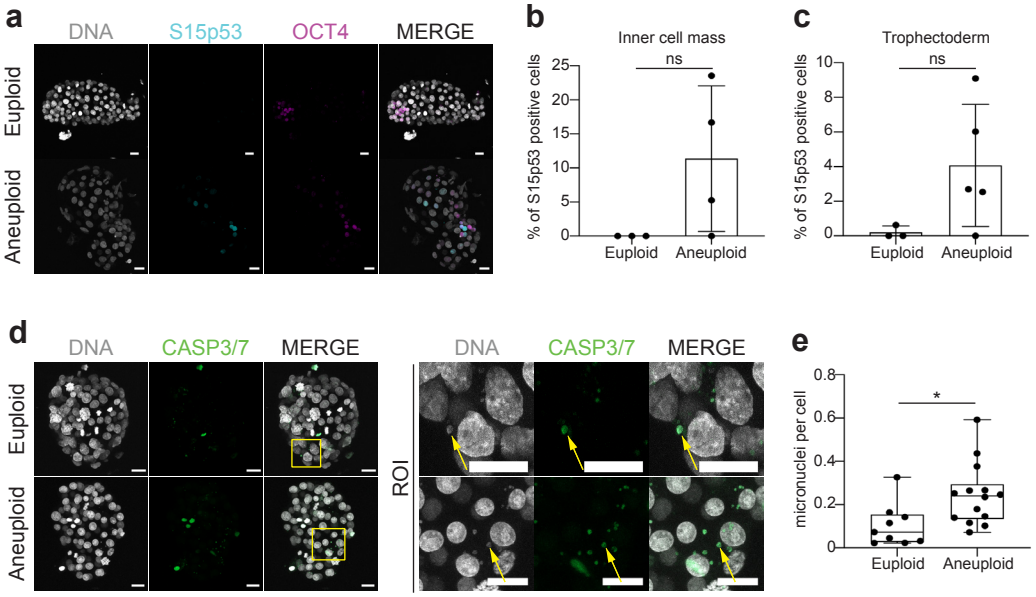
a
DNA
S15p53
OCT4
MERGE
Euploid
Aneuploid
b
Inner cell mass
ns
% of S15p53 positive cells
25
20
15
10
5
0
Euploid
Aneuploid
c
Trophectoderm
ns
% of S15p53 positive cells
10
8
6
4
2
0
Euploid
Aneuploid
d
DNA
CASP3/7
MERGE
Euploid
Aneuploid
ROI
DNA
CASP3/7
MERGE
e
micronuclei per cell
0.8
0.6
0.4
0.2
0
*
Euploid
Aneuploid